The Martian Atmosphere During the Viking Mission, I

Infrared Measurements of Atmospheric Temperatures Revisited

R. John Wilson

Geophysical Fluid Dynamics Laboratory, Princeton, New Jersey
E-mail: rjw@gfdl.gov

and

Mark I. Richardson

Division of Geological and Planetary Sciences, California Institute of Technology, Pasadena, California

The Viking Infrared Thermal Mapper 15-μm channel brightness temperature observations (IRTM T_{15}) provide extensive spatial and temporal coverage of martian atmospheric temperatures on diurnal to seasonal time scales. The 15-μm channel was designed so that these temperatures would be representative of a deep layer of atmosphere centered at 0.5 mb ($\sim$25 km). Our re-examination of the IRTM data indicates that the 15-μm channel was additionally sensitive to surface radiance so that air temperature determinations (nominal T_{15}) are significantly biased when the thermal contrast between the surface and atmosphere is large. This bias is suggested by the strong correlation between the diurnal variation of tropical T_{15} and surface temperatures for non-dust-storm conditions. We show that numerical modeling of the thermal tides provides a basis for distinguishing between the surface and atmospheric contributions to IRTM T_{15} and thus allows the atmospheric component to be estimated. The resulting bias amounts to a $\sim$15-K offset for midday atmospheric temperatures at subsolar latitudes during relatively clear periods and is negligible at night. The proposed temperature correction results in close agreement between the stimulated and observed patterns of diurnal variation for conditions ranging from clear to dusty.

A major consequence of this work is the improved definition of the diurnal, latitudinal, and seasonal variation of martian atmosphere temperatures during the Viking mission. An accounting for the surface temperature bias resolves much of the discrepancy between IRTM and corresponding microwave observations, indicating that there is relatively little interannual variability in global temperatures during the aphelion season ($L_s \sim 40°$–$100°$). We find further support for this argument in a comparison with T_{15} temperatures synthesized from Mariner 9 Infrared Interferometer Spectrometer spectra. The significantly reduced diurnal temperature variations in this season are consistent with the relatively clear atmosphere that is implied by the cooler temperatures. Cooler temperatures and reduced diurnal variation will likely be of significance for the modeling of water ice cloud dynamics in this season. © 2000 Academic Press

1. INTRODUCTION

Viking Infrared Thermal Mapper (IRTM) data provide the foundation for much of our knowledge of the current martian climate. Their utility has ranged from the determination of surface thermophysical properties and polar ice cap composition to the monitoring of dust storm activity and the retrieval of air temperatures and infrared opacity. The IRTM data, which were collected over a period in excess of two Mars years, contain a wealth of information on the spatial and temporal variation of surface and atmospheric temperatures on diurnal to seasonal time scales. The 15-μm channel is of particular interest for atmospheric studies as it was designed to retrieve brightness temperatures (T_{15}) in a deep layer of atmosphere centered at roughly 0.5 mb, corresponding to an elevation of 25 km for typical Mars temperatures. The T_{15} data have shown a significant seasonal modulation of global mean temperature (Leovy 1985, Clancy *et al.* 1996) that is evidently the result of a large seasonal variation in atmospheric dust loading (Zurek *et al.* 1992). The influence of aerosol heating is particularly evident in the rapid increases in global T_{15} temperatures following the onset of each of the two 1977 global dust storms.

The presence of aerosol heating is also revealed by the large diurnal variation in atmospheric temperatures. For example, data obtained by the Mariner 9 Infrared Interferometer Spectrometer (IRIS) instrument during the 1971 global dust storm indicate a strong diurnal temperature variation ($\sim$30 K peak-to-peak) in the summer hemisphere, extending to at least 40 km (Hanel *et al.* 1972b). Comparable diurnal temperature variations (at $\sim$25 km)

555

are evident in the IRTM T_{15} data following the onset of the 1977a and 1977b dust storms (Martin and Kieffer 1979). Even during relatively clear periods, the IRTM T_{15} data indicate a diurnal variation of ~15 K at subsolar latitudes (Martin and Kieffer 1979, Martin 1981, Banfield *et al.* 1996). It is clear that an accounting for diurnal variation is essential for the meaningful comparison of retrieved temperatures from instruments observing the atmosphere at differing local solar times. Thermal tides represent the global-scale thermal and dynamical response of the atmosphere to the diurnal cycle of solar heating. The presence of significant diurnal variability in T_{15} is a strong indication that the thermal tides may be an important component of the martian atmospheric circulation. Moreover, it is evident that an understanding of the thermal tides is essential for the meaningful comparison of retrieved temperatures from instruments observing the atmosphere at differing local solar times.

The comparison of observed and simulated thermal tides provides a useful assessment of both the formulation of thermotidal forcing in a Mars General Circulation Model (MGCM) and the response to this forcing. The IRTM observations provide sufficiently broad coverage in local time and latitude to permit identification of the thermal tides over much of a martian annual cycle. The value of the IRTM data for the study of tides is further enhanced by the availability of simultaneous records of surface pressure, visible opacity, and near-surface air temperature at the two Viking Lander sites. The ability to represent the behavior of surface and atmospheric temperatures as a function of local time will remain a unique strength of the Viking mission data, as observations from the Mars Global Surveyor instruments will, in general, cover a limited range of solar local time.

The present paper is the first of two describing a comparison of IRTM T_{15} temperature and Viking Lander surface pressure data with simulations of diurnal and seasonal variability carried out with an MGCM developed at the Geophysical Fluid Dynamics Laboratory (Wilson and Hamilton 1996). In the course of this investigation, we found that MGCM simulations of the diurnal variation of T_{15} at subsolar latitudes differ significantly from the IRTM T_{15} observations for all but very dusty conditions. Specifically, the observed tropical temperatures are observed to peak at midday while the model simulations indicate a much weaker diurnal variation that peaks at early morning hours. We have examined temperatures provided by other Mars atmospheric modeling groups (Laboratoire de Meteorologie Dynamique, Oxford University, and NASA/Ames) and found this discrepancy is evident in these simulations as well. This fundamental disagreement between observations and model simulations may suggest that there are significant deficiencies in the representation of the Mars atmosphere by MGCMs. Alternatively, the 15-μm channel radiance observations, which are a convolution of atmospheric and surface radiances with the instrument vertical weighting function, may not be properly representative of medieval atmospheric temperatures. The central focus of the current paper is the resolution of this issue. We propose that the differences

in IRTM and simulated T_{15} temperatures are most plausibly accounted for by the existence of a "light leak" in the 15-μm channel so that the observed radiances were contaminated by surface radiation.

The possibility that the IRTM T_{15} data are not representative of 0.5-mb-level temperatures is supported by a comparison of the IRTM data with ground-based microwave profiles of disk-averaged temperatures. The presence of a general 15–20 K offset between the two sets of observations for all non-dust-storm seasons had been ascribed to interannual variation (Clancy *et al.* 1990, 1996). Richardson (1998) showed that the bias is still present in a comparison of simultaneous (May 1980) observations, suggesting that there is an error in either the IRTM or the microwave data (or both). The recent comparison of simultaneous time series of microwave and Mars Global Surveyor Thermal Emission Spectrometer (MGS TES) 0.3-mb temperature observations (Clancy *et al.* 1999) over the period $L_s = 180°–028°$ (October 1997–September 1998) shows an impressive agreement between these two data sets, which strengthens confidence in the microwave measurement technique.

The organization of this paper is as follows. We present the IRTM data in Section 2 and show that T_{15} correlates very strongly with diurnal and longitudinal variations in surface temperature. In Section 3 we use the MGCM and a Linear Tide Model to explore the atmospheric response to a wide range of forcing conditions. We find that the diurnal variation of nominal IRTM T_{15} temperature is inconsistent with theoretical and modeled temperature behavior, as there are substantial differences in magnitude and phasing between the IRTM and model T_{15} temperatures. This provides the basis for distinguishing between surface and atmospheric contributions in the IRTM data. In Section 4 we demonstrate that the observed diurnal T_{15} temperature variation can be accounted for by an additional surface radiance contribution resulting from a leak in the nominal instrument spectral response function. We propose a simple correction scheme for removing the hypothesized surface radiance and show that it leads to a much improved correspondence between IRTM and simulated T_{15} diurnal variability. Comparisons between the IRTM observations and T_{15} temperatures synthesized from the Mariner 9 IRIS spectra are discussed in Section 5. Despite limited local time coverage, the IRIS data suggest distinct deviations from the IRTM data, and agree much better with the predictions of the tidal model discussed in Section 3. The correction also leads to new estimates for the seasonal variation of diurnal average temperatures, which are presented in Section 6. We also discuss the relationship of the IRTM data set with other temperature observations. Our conclusions are summarized in Section 7.

2. IRTM 15- AND 20-μm CHANNEL TEMPERATURE DATA

The IRTM instruments flew aboard the two Viking Orbiters (hereafter referred to as VO1 and VO2), which provided an extensive, but variable, sampling of latitudes, longitudes, and local
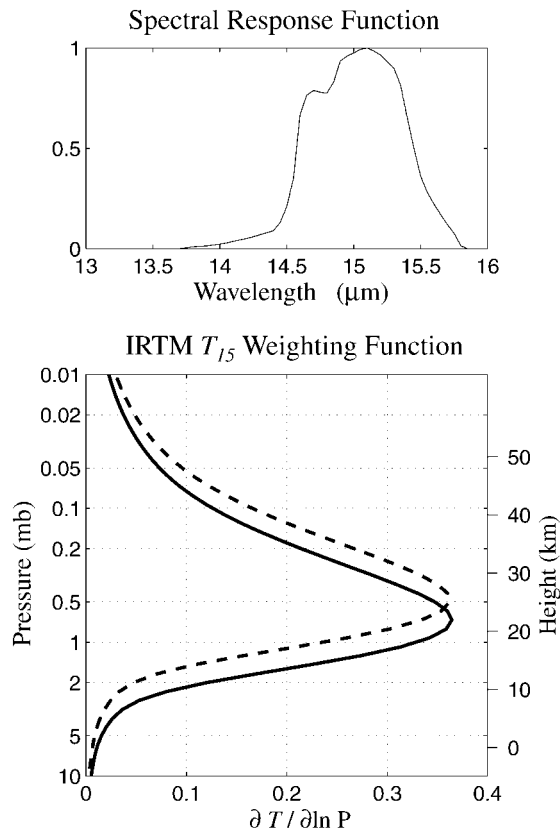
Spectral Response Function

IRTM T_{15} Weighting Function

FIG. 1. (top) The nominal IRTM 15-μm channel spectral response function (Chase *et al.* 1978, Chase, personal communication, 1997). (bottom) The corresponding weighting functions for emission angles of $0°$ (solid line) and $60°$ (dashed line).

times over two Mars years. In this section, we summarize the behavior of atmospheric (T_{15}) and surface temperature as a function of season, latitude, longitude, and local solar time and present comparisons with MGCM simulations. We find that the diurnal variation of observed and simulated T_{15} at equatorial latitudes differs significantly for all but dust-storm conditions. In particular, the IRTM data indicate diurnal and longitudinal variations in T_{15} that are strongly correlated with the corresponding variations in surface temperature, which is in marked contrast with MGCM results.

Each IRTM instrument included a thermopile detector and appropriate filters defining five infrared channels centered at 7, 9, 11, 15, and 20 μm, which yielded corresponding T_7, T_9, T_{11}, T_{15}, and T_{20} brightness temperatures (Chase *et al.* 1978). The 15-μm channel filter was centered on the 15-μm CO_2 absorption feature, and the associated weighting function (Fig. 1) indicates that this channel should be particularly sensitive to radiance emitted from a relatively deep layer of atmosphere centered at the 0.5- to 0.6-mb level. The 7-, 9-, 11-, and 20-μm channels were primarily surface sensing although they displayed differing sensitivities to overlying dust and water ice aerosols (Kieffer and Martin 1979). We use T_{20} as a representation of the surface temperature since these observations share the same

surface footprint as T_{15}, alleviating concerns about mapping spatial temperature variations into apparent differences between the two channels.

The IRTM observations used in this study have been extracted from the Planetary Data System Viking IRTM CD-ROM. The data have been constrained by the quality flag (values between 0 and 4096 are considered good) and by emission angle (we used angles between $0°$ and $60°$, corresponding to accumulated air masses of 1 to 2). We have chosen not to compensate for the weak dependence of the T_{15} weighting function on emission angle (Kieffer *et al.* 1976a) as this would require assumptions about the temperature lapse rate. We have been careful to verify that our conclusions are not dependent on emission angle effects. For general purposes, we have removed observations in the vicinity of volcanoes where the topography is sufficiently high (elevations greater than roughly 12 km corresponding to $\sim$2 mb) that surface emission contributes significantly to the observed 15-μm band radiance.

The evolution of T_{15} over the course of the Viking mission is shown in Fig. 2. The areocentric longitude (L_s) is the Mars seasonal index, running from $0°$ to $360°$ with $0°$ corresponding to vernal equinox, $90°$ to Northern Hemisphere (NH) summer solstice, etc. The available data have been zonally averaged to approximate diurnal average temperatures, although there are biases due to incomplete coverage in longitude and, most significantly, in local time. A limited period of data in the third NH summer is not shown since the diurnal coverage is too sparse for reliably estimating diurnal mean temperatures. The figure reveals a pronounced seasonal modulation in global-mean temperature which corresponds to seasonal variations in atmospheric opacity (Martin 1986, Colburn *et al.* 1989) and solar insolation. The coldest tropical temperatures were observed during the $L_s =$ $30°$–$120°$ period which is centered about aphelion at $L_s = 70°$. The 1977a and 1977b global dust storms (at $L_s = 205°$ and
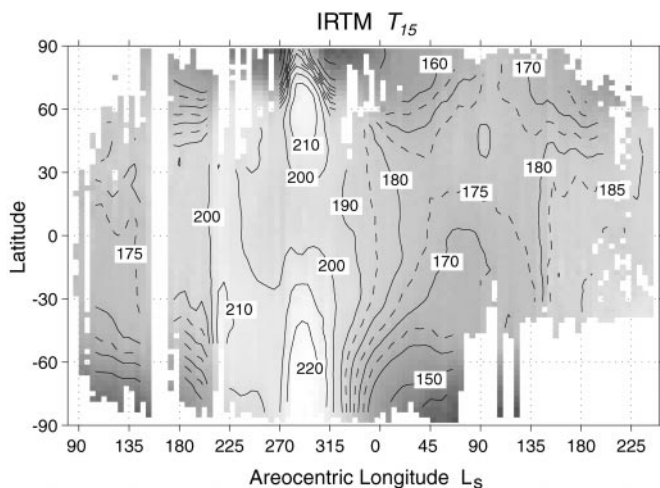
IRTM T_{15}

FIG. 2. The evolution of IRTM T_{15} over the course of the Viking mission. The temperatures represent diurnal averages to the extent possible. Solid contour lines are at intervals of 10 K.

$L_s = 274°$, respectively in the first year) are evident as abrupt temperature increases in the summer (southern) hemisphere. There is also a strong winter polar warming associated with the 1977b global dust storm.

Diurnal Variation

Atmospheric and surface temperatures have previously been shown to vary primarily as a function of latitude and time-of-day (Martin 1981), reflecting the expected dominant influence of seasonal and diurnal variations in solar radiation. For example, Fig. 3 shows the scatter of T_{15} and surface (T_{20}) equatorial (10°S to 10°N) temperatures for late northern hemisphere winter ($L_s = 350°–360°$). The diurnal variation is clearly dominant, although there is considerable scatter in the observations. It is significant to note that much of the scatter is actually associated with longitudinal structure.

FIG. 3. Equatorial (a) IRTM T_{15} and (b) T_{20} temperatures. All observations within latitudes 10°S to 10°N and $L_s = 350°–360°$ are shown. Black (gray) points indicate IRTM data from longitudes with low (high) surface thermal inertia.

The latitude and diurnal variation of T_{15} and T_{20} for late northern hemisphere winter ($L_s = 350°–360°$) and NH spring ($L_s = 30°–40°$) is shown in Fig. 4. The data have been binned by latitude and local solar time so as to average out the presence of stationary waves and longitudinally modulated (non-sun-synchronous) tidal modes. A varying mix of longitudes is sampled for any given latitude and local time bin so that the averaging is only approximate. The striking feature in each channel is the prominent midday temperature maximum at the sub-solar latitude which migrates northward across the equator between these two periods. These panels are similar to those in Plate 1 of Martin (1981), which summarize T_{15} and T_{20} temperatures for a full Mars year. The pattern of variability of T_{15} seen in Fig. 4 is also evident in Figs. 3 and 4 of Banfield *et al.* (1996) for $L_s = 340°–010°$, in Fig. 1a of Martin and Kieffer (1979) for $L_s = 120°–125°$, and in Plate 1 in Richardson (1998). The correlation between T_{15} and T_{20} in the tropics is further emphasized in Fig. 5, which shows equatorial (10°S to 10°N) temperatures for five periods representing non-dust-storm conditions ($L_s = 350°–360°$, 40°–50°, 120°–130°, 180°–190°, and 260°–270°). The T_{15} and T_{20} temperatures are each characterized by a consistent, well-defined diurnal variation, and a strong correlation between T_{15} and T_{20} during daytime hours is clearly evident for each of the periods considered.

By contrast, MGCM simulations with low and moderate dust loading typically indicate a relatively small-amplitude tropical T_{15} variation with an early morning maximum, as indicated by the solid line in Fig. 5. The well-defined minimum in tropical IRTM T_{15} at 2000–2200 LT and the indication of a secondary temperature maximum at 00–0400 LT suggest a general agreement with the MGCM results away from midday and the possibility that the observed midday maximum represents a surface temperature contribution that is not present in the synthetic T_{15} calculation.

The diurnal variations of T_{15} for a period following the 1977a global dust storm and for a period at the height of the 1977b global dust storm are shown in Fig. 6. The atmosphere is considerably warmed by the presence of aerosol, and there is a large diurnal temperature variation in the summer hemisphere, with maximum temperatures occurring in late afternoon. Synthesized T_{15} temperatures from two dust storm simulations carried out with the MGCM are also shown. Some aspects of the 1977b storm simulation, including the realistic simulation of a polar warming that was strikingly evident at this time (Jakosky and Martin 1979), have been discussed by Wilson (1977). Further details will appear in Part II of this study. The simulated temperature patterns appear to capture the character of the observed diurnal variation for the two cases shown. In particular, the amplitude of both the observed and the simulated diurnal tide at high southern latitudes is much larger following the 1977a dust storm than during the stronger 1977b global dust storm. It is noteworthy that the MGCM simulations clearly indicate a dominant semidiurnal variation in the tropical T_{15} temperatures. The good agreement between the observed and simulated T_{15} temperature
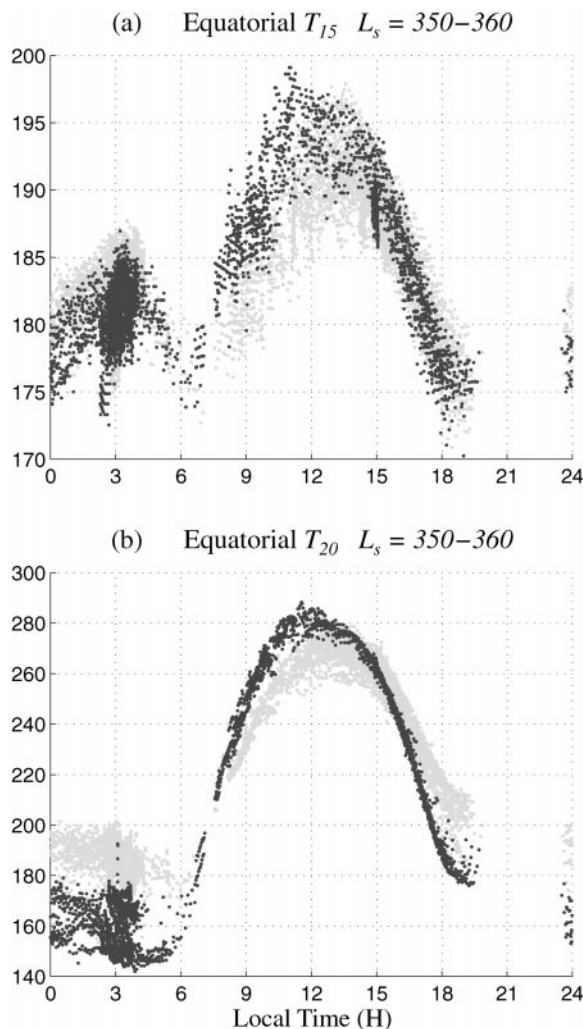
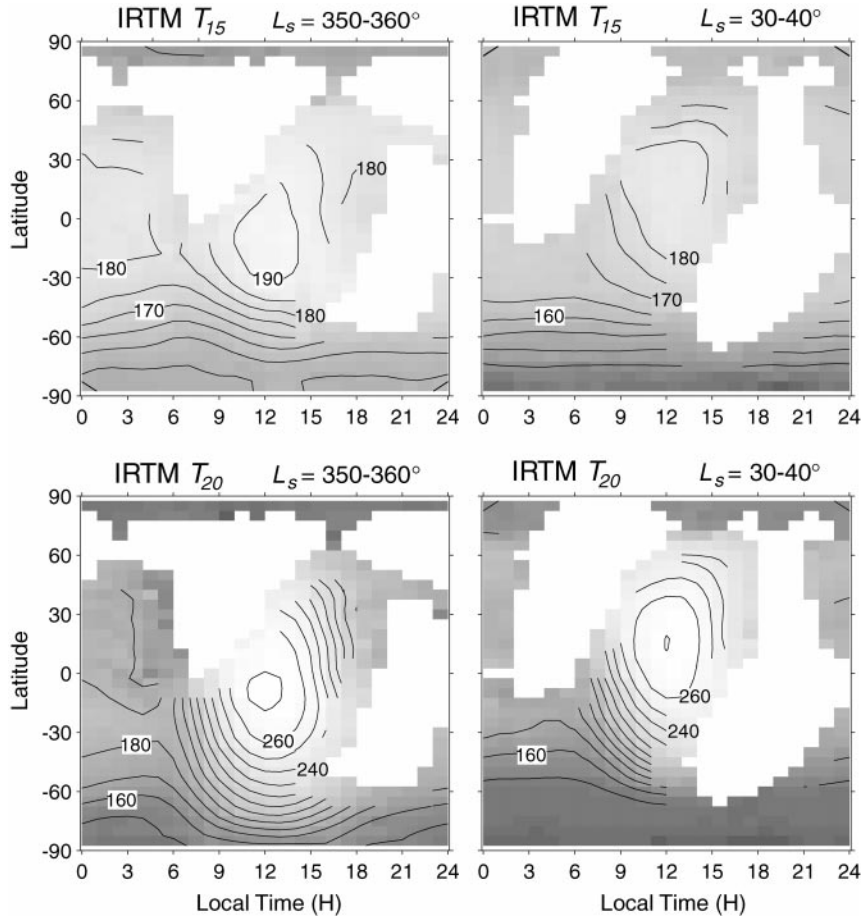**FIG. 4.** IRTM T_{15} (top) and T_{20} (bottom) temperatures plotted as a function of latitude and local time for the periods $L_s = 350°–360°$ (left) and $L_s = 30°–40°$ (right). T_{15} and T_{20} temperatures are contoured in 5 and 10 K intervals, respectively. The data have been binned at a resolution of 5° of latitude and 1 h of local time where an hour is 1/24 of a Mars solar day.

patterns demonstrates the utility of the MGCM for interpolating/extrapolating the IRTM data in latitude and time of day.

Expected Surface Sensitivity

The strong correlation between T_{15} and T_{20} motivates a consideration of the expected sensitivity of the nominal 15-μm channel to surface and boundary-layer radiance. Figure 7 shows the influence of surface temperature on retrieved T_{15} as a function of surface pressure. For simplicity, an isothermal (170 K) atmosphere is assumed although the variable height of the imposed surface temperature may be taken to represent the combined influence of a surface and boundary layer. The change in T_{15} is less than 0.5 K as the imposed surface temperature at 6 mb varies from 180 to 280 K. The T_{15} variation remains less than 5 K when the imposed temperature variation extends to 3.5 mb (roughly 5 km above the nominal surface). We find that more realistic boundary layer temperature profiles yield T_{15} variations of less than 1.5 K. The sensitivity of T_{15} to variations in surface temperature is decreased for warmer or more realistic stratified temperature profiles when the surface radiance con-

tribution represents a smaller fraction of the total radiance due to the nonlinearity of the Planck function. Similarly, T_{15} is even less sensitive to variations in atmospheric temperature at heights well above 0.5 mb due to the lack of infrared emissivity and the relatively low atmospheric temperatures in this region.

Spatial Temperature Correlations

The martian surface thermal inertia, albedo, and topography all have considerable longitudinal variability, and it is natural to look for these influences on the observed surface and T_{15} temperatures. In fact, longitudinal variations in pre-dawn surface temperatures (T_{20}) are the basis for deriving the spatial pattern of the thermal inertia field (Palluconi and Kieffer 1981). For example, the large range in early-morning T_{20} temperatures in Fig. 3 is a reflection of variable surface thermal inertia. The thermal inertia field at tropical to northern midlatitudes (10°S to 50°N) has a prominent zonal wavenumber 2 pattern that is largely independent of latitude. The surface thermal inertia and albedo fields tend to be inversely correlated (Christensen and Moore 1992), and thus their effects partially compensate each
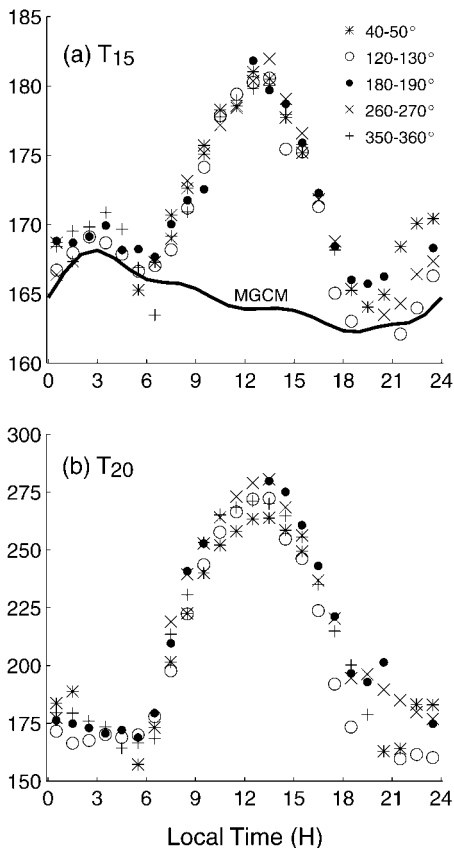
FIG. 5. Equatorial (10°S to 10°N) IRTM T_{15} temperatures plotted as a function of local time for five relatively clear periods. Seasonal variations in the diurnal-mean tropical temperature have been removed by subtracting a seasonally varying offset temperature: $L_s = 40°$–$50°$ (0 K offset), $120°$–$130°$ (4 K offset), $180°$–$190°$ (20 K offset), $260°$–$270°$ (20 K offset), and $350°$–$360°$ (12 K offset). The solid line indicates a representative synthetic T_{15} variation (12 K offset) calculated from an MGCM simulation for $L_s = 355°$. (b) Diurnal variation of equatorial IRTM T_{20} temperature.

other in determining the maximum (midday) surface temperature. The effect of variable surface thermal inertia is dominant, however, so that, for a given latitude, midday T_{20} temperatures are strongly (inversely) correlated with surface thermal inertia. This results in a zonal variation in midday T_{20} that is relatively uniform in this latitude range during late NH spring and summer.

Figure 8 shows the modulation of midday (1200–1400 LT) T_{15} and T_{20} temperatures within the 20°–30°N latitude band during NH spring ($L_s = 60°$–$90°$). The zonal wave 2 pattern and the close correlation between T_{15} and T_{20} hold for other latitude bands from 10°S to 50°N. There is relatively little zonal variation in topography in the low-lying (0–2 km elevation) latitude bands of 30°–40°N and 40°–50°N compared with lower latitudes (10°S to 20°N) where the elevated terrain of the Tharsis shield is prominent. We interpret the comparable correlation between T_{15} and T_{20} within different latitude bands as suggesting that longitudinal variations in T_{15} reflect variations in surface temperature (which is modulated by the surface thermal inertia)

independent of the pressure level (topographic elevation) from which the surface radiates.

Figure 9 shows the latitudinal variation of T_{15} and T_{20} for three VO2 orbits which passed over or near Arsia Mons on consecutive sols during NH spring ($L_s = 52.5°$–$53.5°$). The local times range from 1118 to 1148 LT and, at each latitude, are within 0.1 H of each other. The correlated increase of T_{15} and T_{20} with latitude (10 and 40 K, respectively) is roughly consistent with the correlated diurnal variation of T_{15} and T_{20} in Figs. 5 and 8. Significantly, there is little dependence of T_{15} on topography for elevations below 13 km. This is particularly evident in the lack of temperature variation for the orbit that passed over the western flank of Olympus Mons ($\sim$13 km). The sharp increase in T_{15} in the vicinity of Arsia Mons reflects the increasing contribution of surface radiance within the lower portion of the weighting function. The T_{15} temperatures sharply increase at elevations above 15 km, reaching values of over 195 K at the summit of Arsia Mons at roughly 20 km elevation.

Scans from other volcano passages show a similar T_{15} dependence on surface elevation. Figure 10 shows T_{15} as a function of elevation for a series of VO1 scans that passed over or near Arsia Mons, Pavonis Mons, and Olympus Mons at $L_s \sim 139°$. These observations all fall within the 1100–1330 LT interval, and the surface temperatures generally lie within the range 280–285 K. It can be seen that there is little dependence of T_{15} on elevation for elevations below 13 km ($\sim$1.8 mb). The T_{15} temperatures sharply increase for elevations above 15 km, reaching values of $\sim$205 K at the summit of Arsia Mons ($\sim$20 km) and 225 K near the summit of Olympus Mons. This rapid increase in the influence of surface temperature with topographic height is essentially consistent with Fig. 7.

The volcano scan data suggests that there is relatively little *differential* transmission of radiation emitted from pressures greater than 2 mb and that the radiance contribution to T_{15} sharply increases between 2 and 1 mb as suggested by the nominal weighting function (Fig. 1). We emphasize, however, that these data do not rule out the possibility of a surface radiance contribution that is effectively independent of the emission pressure level. We have shown that the nominal spectral response function leads to a T_{15} that is quite insensitive to surface and boundary-layer radiance (see Fig. 7). In Section 4 we suggest how the *actual* spectral response function could allow surface radiance to make a significant contribution to the observed radiance, independent of surface pressure.

3. ATMOSPHERIC THERMAL TIDES

We now consider the simulation of atmospheric and surface temperatures and examine how these relate to the diurnal variation of T_{15} temperature. The models used in previous studies of diurnal variability in the martian atmosphere have ranged from one-dimensional thermal balance models (e.g., Gierasch and Goody 1968, Pollack *et al.* 1979, Colburn *et al.* 1989) to models that represent the fundamentally three-dimensional structure of
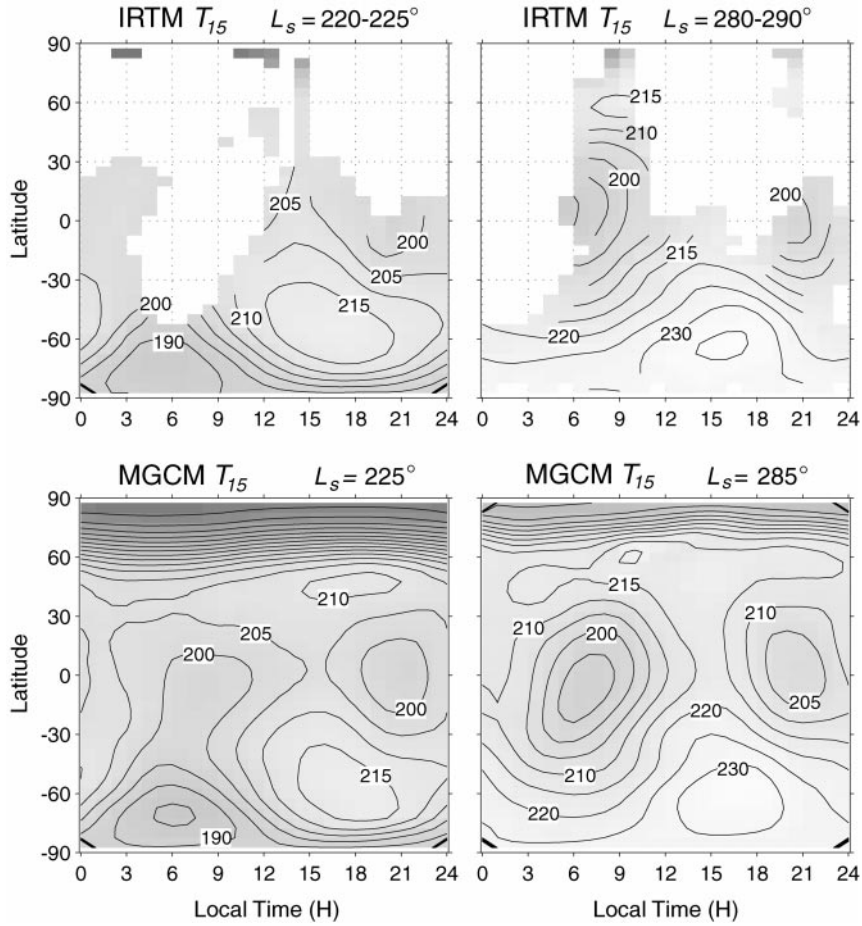
FIG. 6. IRTM T_{15} temperatures plotted as a function of latitude and local time for two dust storm periods: (top left) $L_s = 220°–225°$ following the 1977a global dust storm and (top right) $L_s = 285°–290°$ during the 1977b global dust storm. The bottom panels show corresponding temperatures from two MGCM dust storm simulations.
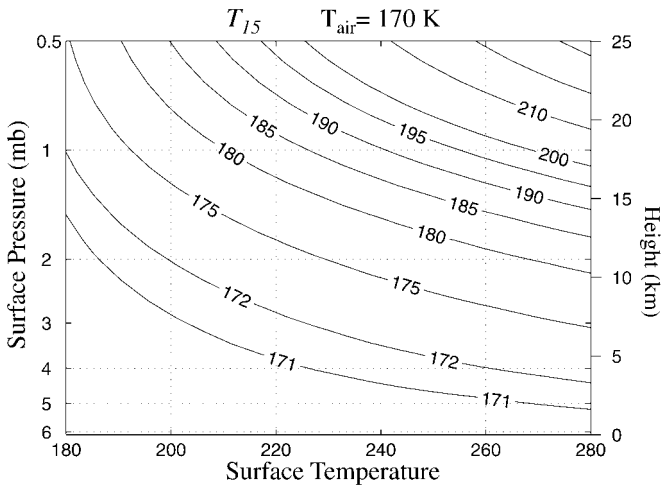

FIG. 7. Synthetic T_{15} temperature calculated for an isothermal 170 K atmosphere overlying a surface with variable temperature and elevation. The height axis indicates elevation above the nominal 6-mb surface.
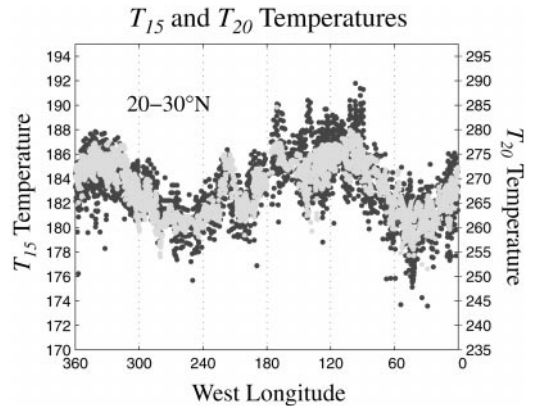

FIG. 8. Longitudinal variation of midday (1200–1400 LT) T_{20} (gray) and T_{15} (black) temperatures within the 20°–30°N latitude band during late NH spring ($L_s = 60°–90°$).
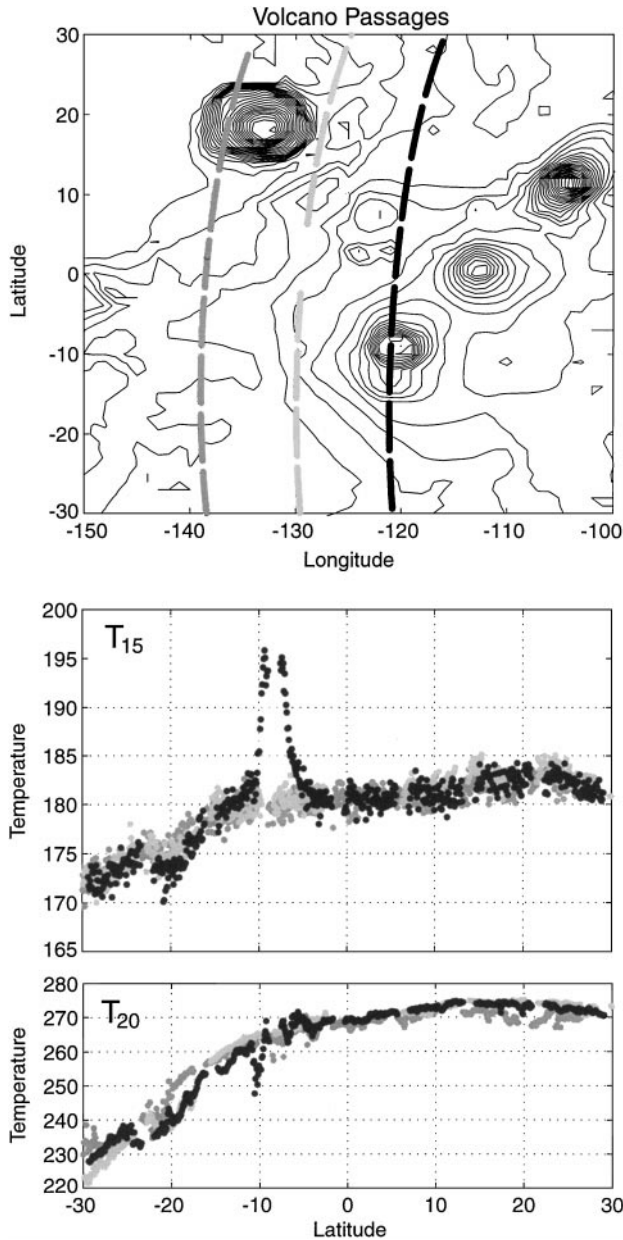
FIG. 9. (top) A sequence of three consecutive VO2 scans which passed over or near Aria Mons at $L_s = 53.4°$. The observations shown were collected at 1130 LT. The topographic contours are from the USGS $1° \times 1°$ Digital Terrain Model data set and are plotted at 1-km intervals. The latitudinal variation of T_{15} and T_{20} is shown in the middle and bottom panels, respectively. Black dots indicate temperatures corresponding to the orbit that passed directly over Arsia Mons.

the thermal tides (Zurek *et al.* 1976, Leovy and Zurek 1979, Wilson and Hamilton 1996). Thermal tides are the global-scale oscillations of temperature, wind, and surface pressure that arise in response to the diurnal cycle of solar heating. A brief review of aspects of tide theory is given in the Appendix. The dynamical response of the atmosphere to applied heating is particularly important in the tropics, where the diurnal tide has the character

of a vertically propagating gravity wave. The purpose of this section is to illustrate the behavior of the thermal tides and to demonstrate that the observed diurnal variation in equatorial T_{15} (Fig. 5) is robustly inconsistent with expectations derived from modeling the thermal tide. This result will be used to provide the basis for estimating the surface radiance bias in the IRTM T_{15} observations.

One-dimensional models provide a reasonable simulation of the surface and near-surface (1.0–1.6 m) temperatures at the Viking and Pathfinder Lander sites (Savijarvi 1995, 1999). Surface temperatures peak around 1230–1330 LT (Fig. 5) due to the relatively low surface thermal inertia. Near-surface Viking Lander (1.6 m) air temperatures are observed to peak at 1400–1500 LT (Hess *et al.* 1976), and observations at the Pathfinder Lander site indicate a temperature maximum (1.0 m) at 1415 LT (Schofield *et al.* 1997). Modeling results (e.g., Gierasch and Goody 1968, Pollack *et al.* 1979) indicate that the local time of the atmospheric temperature maximum rapidly tends toward 1800 LT away from the surface. The absence of a phase lag between the observed T_{15} and T_{20} tropical temperatures (Fig. 5) clearly indicates that the observed behavior is not readily interpreted by 1-D modeling. The presence of a semidiurnal T_{15} variation in the tropics during dusty periods (Fig. 6) emphasizes the limitations of 1-D modeling as this effect is fundamentally a consequence of the dynamical response of the atmosphere.

In the following, we will examine the atmospheric temperature response to a range of thermal forcing scenarios. The model physics incorporated in MGCMs account for the absorption and emission of short- and long-wave radiation by gaseous CO_2 and aerosols, heat conduction into the soil, sensible heat exchange between the surface and the atmosphere, and turbulent or
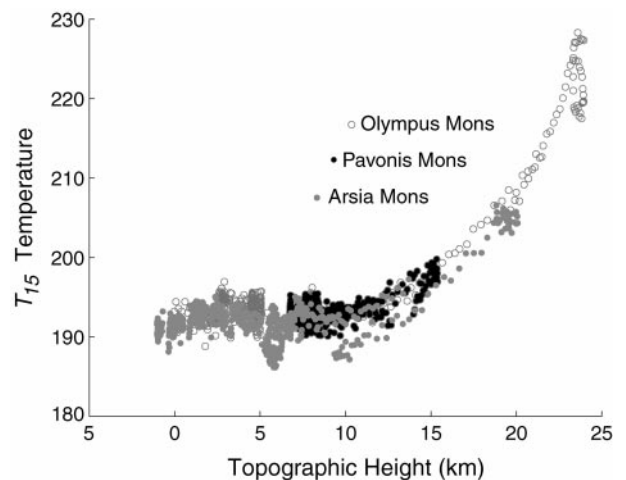

FIG. 10. Plot of T_{15} as a function of topographic elevation for a series of VO1 orbits in the Tharsis region (10°S to 30°N, 100°W to 150°W) for $L_s = 139°$. The local times range from 1100 to 1300 LT, and the surface temperatures are generally in the range 280–285 K. The lower branch of temperatures for Arsia Mons between 10 and 15 km correspond to distinctly lower surface temperatures than for the upper branch. The topographic heights have been interpolated from the USGS $1° \times 1°$ Digital Terrain Model data set.

convective heat exchange within the atmosphere due to eddy and convective mixing processes. We have formulated a Linear Tide Model (LTM) to complement the more detailed MGCM by providing greater scope for generalizing the specification of thermal forcing and for investigating the influence of the zonal mean temperature and zonal wind fields on the atmospheric response.

Zurek and Leovy (1981) have shown that tide models can be used to relate the amplitude of the semidiurnal surface pressure signal at the Viking Lander 1 site to the atmospheric heating resulting from the absorption of solar radiation by aerosol. Thus, the observed semidiurnal tide can serve as an additional, independent constraint on the thermotidal forcing, and tide modeling provides a means of relating this forcing to both atmospheric temperature and surface pressure variations.

The Linear Tidal Model

The LTM represents the primitive equations of motion on a sphere, linearized about a zonally symmetric basic state. The model is formulated with a terrain-following sigma coordinate in the vertical which allows for the incorporation of meridionally varying topography. The solution is represented by a spectral expansion in the zonal direction, and finite differences are employed for calculating meridional and vertical derivatives. The basic-state zonal-mean temperature and zonal wind fields may be specified as functions of height and latitude. The LTM is time-marched until a steady-state tidal response is achieved. By allowing for the incorporation of topography and basic-state zonal-mean temperature and winds, the LTM relaxes some of the assumptions of classical tidal theory (e.g., Chapman and Lindzen 1970). The model results presented here are calculated on a uniform latitude grid with $5°$ resolution and 40 sigma levels extending to roughly 88 km. This is the same model resolution used in the MGCM (Wilson and Hamilton 1996). Additional calculations indicate that the following results are insensitive to increases in either the horizontal or the vertical resolution.

The thermal forcing for the LTM is specified as a combination of boundary-layer heating and dust-induced solar heating. The thermotidal forcing is decomposed into harmonics of the solar day which are then used to force the corresponding sun-synchronous zonal wavenumbers of the linear model. In the following, we focus on the diurnal and semidiurnal tides, as MGCM simulations indicate that the tidal response is well characterized by the diurnal and semidiurnal harmonics. We will hereafter follow the convention of describing diurnal and semidiurnal variations of a field, X (where X may be surface pressure, P, air temperature, T, etc.), as $S_1(X)$ and $S_2(X)$, respectively.

The boundary-layer component of the thermotidal forcing is intended to account for radiative, convective, and sensible heat transfer from the surface and within the boundary layer. Gierasch and Goody (1968) presented 1-D model simulations that showed that diurnal temperature variations are largely confined to a relatively shallow (<5 km) layer of atmosphere for clear-sky conditions. They also showed that while different formulations of the boundary layer heat flux had a significant ef-

fect on the diurnal-mean temperature profile, these formulations had little influence on the diurnal temperature variation above a couple of kilometers. These variations would be expected to have negligible influence (~1.5 K) on the diurnal variation of T_{15} (~1.5 K) as has been confirmed in our calculations. A fairly realistic representation of boundary-layer heating in the LTM for relatively clear sky conditions may be obtained from a set of parallel 1-D model calculations corresponding to each of the model latitudes. Alternatively, this heating has also been idealized as an exponentially decaying function in the vertical as in other tide studies (Hess *et al.* 1977, Leovy and Zurek 1979). This idealized formulation allows for the specification of a phase shift with height to stimulate convective heat transfer from the surface.

The heating due to the scattering and absorption of solar radiation by dust is calculated using the subroutines employed in the MGCM (Wilson and Hamilton 1996). The degree of absorption for a given extinction optical depth of dust is dependent on the assumed optical properties, most significantly the single-scattering albedo, ω. At present there is some uncertainty in this quantity, with estimates ranging from 0.86 (Pollack *et al.* 1979) to 0.92 (Clancy and Lee 1991). This can lead to considerable variation in atmospheric heating (which varies as $1-\omega$) for a fixed extinction optical depth. The calculations presented here employ $\omega = 0.875$. The aerosol distribution may be arbitrarily specified in latitude and height, but it is typically assumed to be uniformly mixed to some specified height. Aerosol heating is a simple function of the solar zenith angle; hence it will be expected to maximize at noon. Aerosol heating has a stabilizing influence on the atmosphere so that the depth of heating by convection is expected to decrease with increasing aerosol opacity. The absorption of solar insolation by gaseous CO_2 has also been included and has been found to have little influence on the tidal fields of the lower atmosphere (<35 km). Pollack *et al.* (1979) have shown that the diurnal variation of atmospheric temperature is relatively insensitive to the effective emissivity of the aerosol. Consequently, it is sufficient to employ a Newtonian damping of temperature perturbations to simulate the radiative relaxation back to the zonal mean basic state temperature. We have used damping times ranging from 0.5 to 4.0 days, with a typical value of 1 day.

Linear Tidal Model Experiments

The character of the thermal tide may be illustrated by considering the results from two simulations using the MGCM and the Linear Tidal Model. The MGCM simulation is intended to be representative of the late northern hemisphere winter ($L_s = 355°$) season and employs a dust distribution that is nonuniformly mixed in latitude, with a tropical column optical depth of ~0.8. The zonal-mean temperature and zonal wind fields are characterized by relatively cool polar latitudes and associated midlatitude westerlies (Santee and Crisp 1993, Haberle *et al.* 1993). The LTM calculation employs a uniformly mixed aerosol distribution (to 35 km) with a column optical depth of
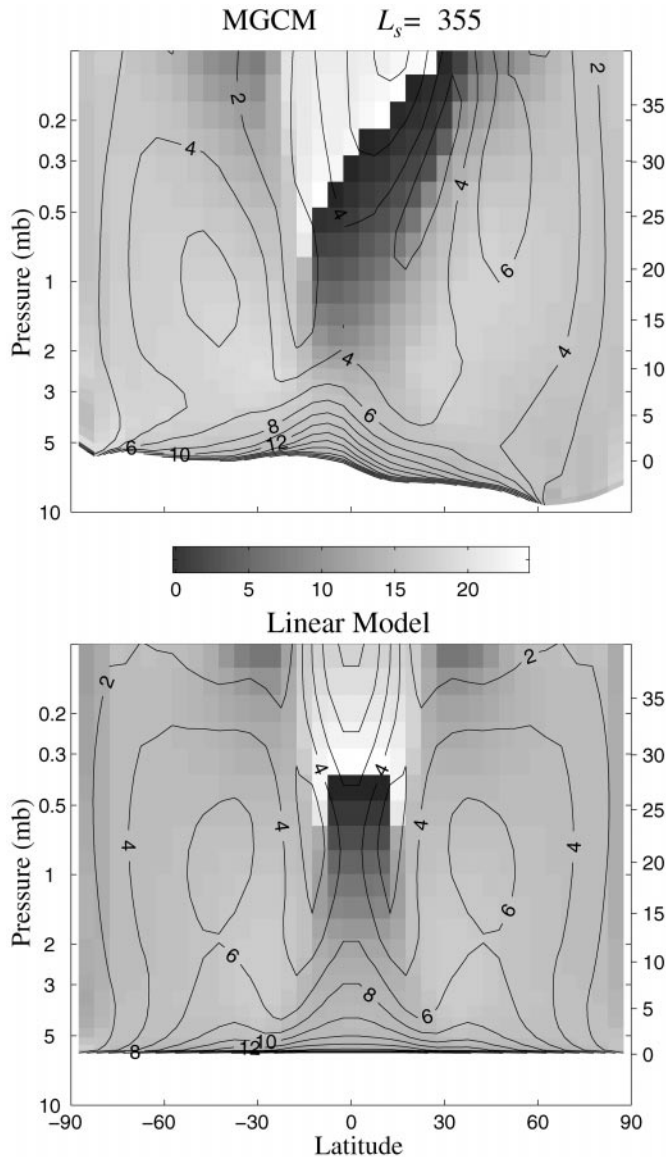
FIG. 11. Height and latitude variation of the amplitude and phase of the sun-synchronous, diurnal period atmospheric temperature response as simulated by the MGCM and the Linear Tidal Model. Tidal amplitudes are contoured in increments of 2 K. The phase of the temperature maximum is indicated by the shading, which ranges over 24 h.

$\tau = 0.8$, realistic boundary layer heating, and solar insolation appropriate for equinox. The basic state is prescribed as a resting atmosphere, with flat topography and a meridionally uniform, vertically varying zonal-mean temperature field.

Figure 11 shows latitude–height cross sections of the phase and amplitude of $S_1(T)$ for the MGCM and LTM simulations. There is a close correspondence between the two simulations, indicating that the LTM approximates the more comprehensive MGCM reasonably well. The difference between the two boundary-layer responses is largely due to the presence of longitudinal topographic variations in the MGCM simulation. The

latitudinal asymmetry in the MGCM tide response is due to the presence of relatively stronger westerlies in the northern hemisphere.

The temperature response is particularly strong near the surface, in agreement with 1-D model calculations (Gierasch and Goody 1968, Pollack *et al.* 1979). In midlatitudes, the phase of $S_1(T)$ shows very little variation with height, and the amplitude is largely a direct response to aerosol heating. The diurnal variation at $45°$ latitude in the LTM simulation ($\sim$12 K peak-to-peak) at 20 km is consistent with 1-D model predictions (Pollack *et al.* 1979, Fig. 9) and yields an equivalent T_{15} variation of $\sim$10 K. Most significantly, the time of temperature maximum in these simulations is 1800 LT, which is distinctly later than for the tropical temperatures shown in Figs. 4 and 5. By contrast, the phase of the tropical temperature response varies strongly with height, indicating a vertically propagating tide component with a vertical wavelength of $\sim$30 km. At roughly 25 km in height, the local time of diurnal tide temperature maximum has advanced to early morning. The tropical T_{15} variation for the MGCM simulation, which is dominated by contributions from $S_1(T)$, is shown in Fig. 5. As expected from classical tidal theory, the semidiurnal tide (not shown) shows relatively little phase variation with height within the tropics, and the amplitude of $S_2(T)$ is significantly weaker than that of $S_1(T)$.

Effects of Aerosol

Figures 12 to 15 summarize results from a series of simulations in which we varied the column optical depth from 0 to 5. The aerosol was uniformly distributed to 35 km, and a realistic boundary layer forcing was used for these calculations. A basic state representative of equinoctial conditions is also employed. It should be noted that these calculations use a fixed zonal-mean basic state while, in actuality, the basic state would be strongly influenced by increased solar heating in the dusty simulations. We have found that the tide response is relatively unaffected by changes in the thermal structure but is more significantly influenced by changes in the zonal-mean zonal flow.

The altitude and local time variation of equatorial temperature for simulations with aerosol optical depths of 0, 0.5, 1, and 5 are shown in Fig. 12. The tropical temperature variation is dominated by the vertically propagating diurnal thermal tide. The phase variation with height is not dependent on the dust optical depth, nor is it sensitive to the vertical distribution of the dust (not shown). The semidiurnal temperature variation is seen to make an increasingly prominent contribution to the total temperature variation as the aerosol heating is increased.

Figure 13 shows the resulting T_{15} fields as functions of latitude and local time. Equatorial sections of T_{15} are shown in Fig. 14. Clearly evident in the simulations is the absence of the subsolar temperature maximum so prominent in the IRTM observations shown in Figs. 4 and 5. The 15-μm weighting function (Fig. 1) integrates over a significant fraction of the vertical wavelength of the tropical $S_1(T)$ component, leading to substantial cancellation and a relatively small contribution to T_{15}. The semidiurnal tide
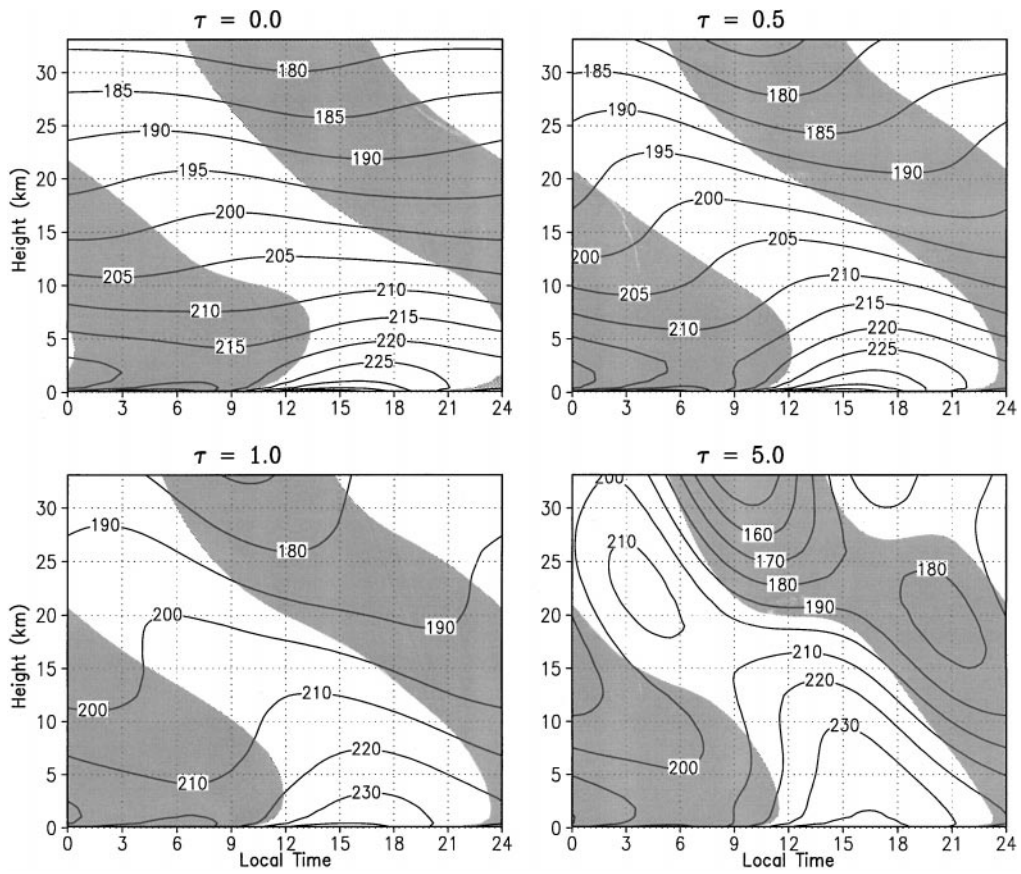
FIG. 12. Height and local time dependence of equatorial temperature as simulated by the Linear Tidal Model. The thermotidal forcing is a combination of realistic near-surface heating and heating due to aerosol with column optical depth, τ, of 0, 0.5, 1.0, and 5. The aerosol is uniformly mixed in latitude and extends to roughly 35 km. Temperatures are in degrees K. Shading indicates regions of negative temperature deviation from the diurnal mean.
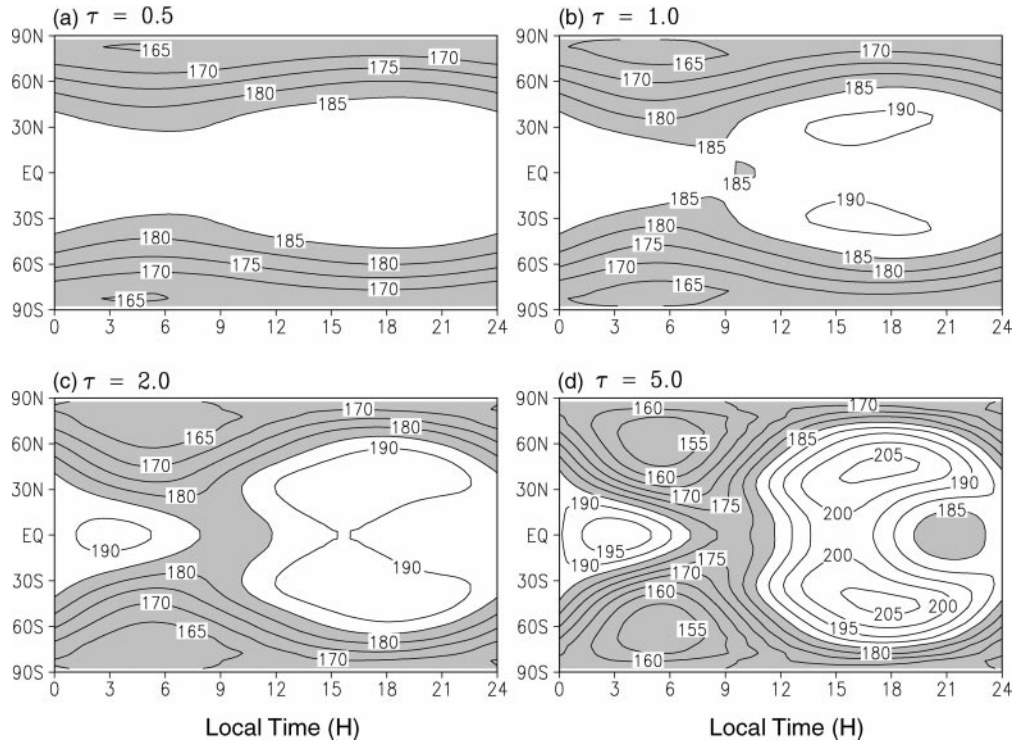

FIG. 13. Simulated T_{15} plotted as a function of latitude and local time for four dust optical depths. The simulations correspond to those described for Fig. 12.
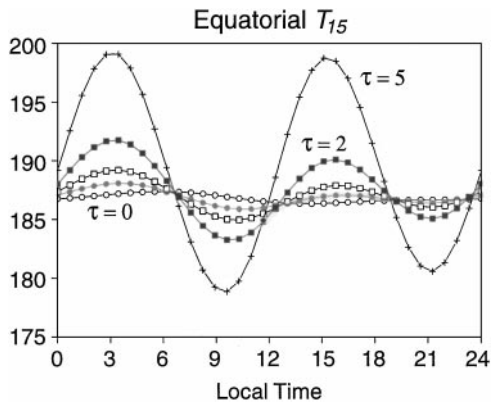
FIG. 14. Simulated equatorial T_{15} temperature plotted as a function of local time for five dust optical depth cases, τ, of 0, 0.5, 1, 2, and 5. The simulations correspond to those described for Fig. 12.

exhibits a relatively modest phase variation with height which allows for a more efficient contribution to the T_{15} observation. At moderate optical depths ($\tau > 1$), $S_2(T_{15})$ emerges as the dominant component of the tropical T_{15} signal. This pattern of behavior is consistent with the tendency for the semidiurnal surface pressure signal, $S_2(p)$, to dominate the $S_1(p)$ signal for increasing optical depth (Wilson and Hamilton 1996). The presence of $S_2(T_{15})$ is clearly evident in the observations during the global dust storm periods shown in Fig. 6.

Figure 13 indicates that the extratropical temperature response is dominated by $S_1(T)$. The amplitude is roughly proportional to the layer aerosol optical depth in the vicinity of the 0.5-mb level, as the boundary-layer heating makes little contribution to T_{15} at these heights and latitudes.
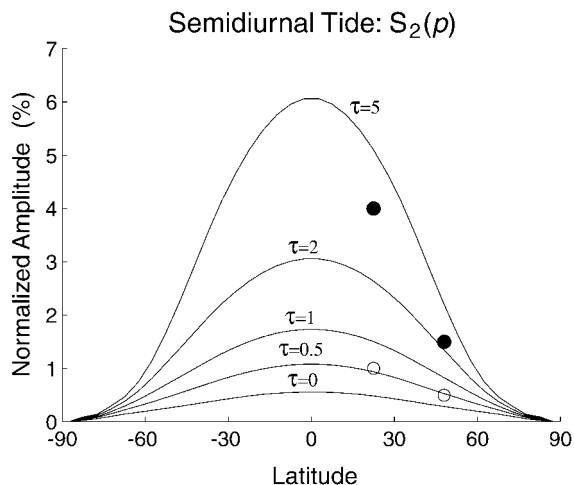

FIG. 15. Amplitudes of the semidiurnal pressure variation, $S_2(p)$, for the simulations shown in Figs. 12–14. The amplitudes have been normalized by the (in this case, meridionally constant) surface pressure so that the tidal amplitude is expressed as a percentage of the mean surface pressure. Open circles indicate typical observed values at the VL1 (22.5°N) and VL2 (48°N) sites during relatively clear periods, and filled circles correspond to tide amplitudes at VL1 and VL2 during the 1977b global dust storm.

We have also examined the influence of stronger and deeper representations of the boundary-layer heating in the LTM and found that they have very little impact on extratropical temperatures well away (~8 km) from the surface. This is consistent with the expectation that the extratropical tide response is vertically trapped and responds to local (in height) heating. By contrast, the horizontal response is quite nonlocal and is not particularly sensitive to horizontal variations in the thermotidal forcing. The vertically propagating response in the tropics is strengthened by increased boundary-layer heating, but the phase variation remains effectively unchanged. The effect of deep boundary layer heating, as might result from the deep penetration of convective mixing, is evidently more than offset by the associated dynamic cooling due to the vertically propagating tide. The dynamic response is able to dominate the local thermal heating due to the tendency for tide amplitude to increase with height as the atmospheric density decreases. In summary, the vertically trapped nature of the extratropical tide response and the invariance of the phase variation of the propagating tropical tide lead to the result that the T_{15} response to boundary-layer heating is quite weak.

Similar integrations have been carried out with different damping rates and vertical profiles for the Newtonian cooling. The extratropical tidal response is effectively insensitive to the thermal damping employed, as expected of vertically trapped modes. The amplitude of the vertically propagating, tropical diurnal response does increase with increasing damping time, but the pattern of variation remains virtually identical to that shown in Fig. 12. As a consequence, the amplitude of the T_{15} response remains small and the phase is unchanged. The vertically propagating semidiurnal tide is found to be relatively insensitive to the imposed thermal damping time scale due to its great vertical wavelength.

Surface Pressure Oscillations

We now consider a comparison of the simulated semidiurnal surface pressure oscillations with those calculated from the Viking Lander surface pressure record. The latitude variation of the amplitude of $S_2(p)$ for the five LTM simulations discussed above is shown in Fig. 15. These amplitudes have been normalized by the diurnal-mean surface pressure to facilitate comparison with data from the Viking landers, which are also indicated in the figure (see Wilson and Hamilton 1996). The heating due to a dust optical depth of $\tau = 5$ yields a normalized $S_2(p)$ amplitude reasonably consistent with the highest values observed during global dust storms (about 4% at the VL1 site at 22.5N, following the initiation of the 1977a and 1977b storms), and thus it represents an upper limit on dust heating in the martian atmosphere. These simulations suggest that the Viking Lander equinoctial $S_2(p)$ amplitudes correspond to heating due to optical depth between 0.5 and 1. It should be noted that the use of a larger single-scattering albedo (we used $\omega = 0.87$) will yield less heating and weaker $S_2(p)$ amplitudes for the same optical depth. The very low $S_2(p)$ amplitudes observed during NH summer are evidently due to interference with non-sun-synchronous

tide modes (Wilson and Hamilton 1996) and are likely not representative of the sun-synchronous tide component which is being modeled here. It can be seen that the stimulated range of $S_2(p)$ amplitudes compares well with the observed range of $S_2(p)$ amplitudes for a realistic set of optical depths.

The simulated $S_2(p)$ amplitude is fairly insensitive to the vertical distribution of dust. Simulations with different zonal-mean surface pressure distributions also indicate that the normalized $S_2(p)$ response is relatively insensitive to changes in topography and undergoes modest variations in shape with changes in the zonal-mean zonal flow. The robustness of the $S_2(p)$ response indicates that this observations may serve as a useful constraint on column-integrated atmospheric heating. By contrast, $S_1(p)$ is sensitive to both the vertical distribution of aerosol and the meridional variation in zonal mean topography. Our formulation of the thermotidal forcing for both relatively clear ($\tau \sim 0.5$–1) and dusty ($\tau \sim 5$) conditions leads to simulated semidiurnal surface pressure oscillations consistent with the Viking Lander pressure observations. It would be difficult to construct a scenario with significantly enhanced thermotidal forcing and a large atmospheric temperature response without a corresponding increase in the amplitude of $S_2(p)$.

MGCM Comparisons

The LTM tide results shown in Fig. 12 are in good agreement with MGCM simulations for low to moderate dust loading. The top panel of Fig. 16 shows the variation of equatorial temperature with height and local time from the MGCM equinoctial ($L_s = 355°$) simulation with moderate ($\tau \sim 0.8$) dust loading. A height–latitude section of $S_1(T)$ for this simulation is shown in Fig. 11, and the corresponding tropical T_{15} variation (with temperature offset) is shown in Fig. 5. The pattern of temperature response for stronger thermal forcing remains similar in the two models, although there are increasing differences in detail. In particular, the LTM does not represent wave breaking resulting from the development of regions of convective and/or shear instability associated with low local Richardson numbers. The pressure levels and local times for which these processes become effective will vary with the strength of the thermal forcing, as has been discussed by Zurek (1976). For example, the temperature distribution shown on the lower right of Fig. 12 ($\tau = 5$) is convectively unstable at mid-morning above 20 km. It should again be noted that the basic state employed in Fig. 12 does not reflect changes in thermal structure due to the increased dustiness.

We now discuss the two MGCM dust storm simulations for which maps of T_{15} were shown in Fig. 6. The aerosol in these calculations is deeply distributed, with optical depths of roughly 3 and 5 for the 1977a and 1977b cases, respectively. The cross sections of equatorial temperature in Figs. 16b and 16c show a large $S_2(T)$ response, particularly for the 1977b storm simulation. This temperature variation leads to significant early-morning and early-afternoon temperature (1500 LT) maxima with little phase variation with height. The resulting equatorial $S_2(T_{15})$ are consistent with those for the LTM simulations shown
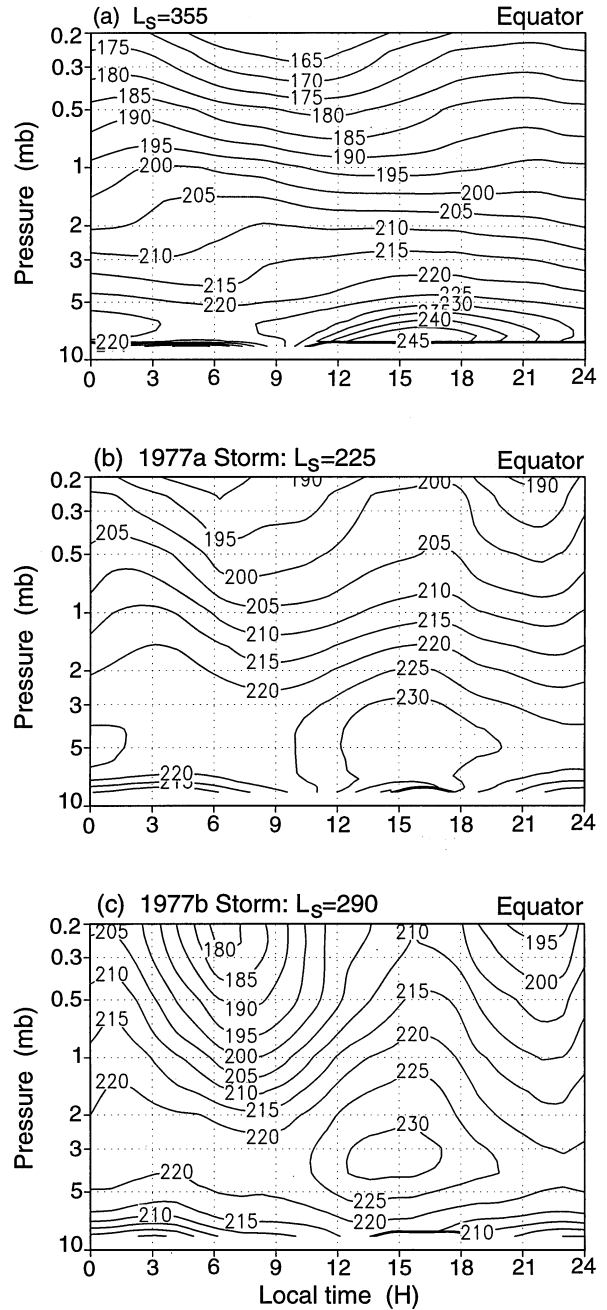

FIG. 16. MGCM simulations of the height and local time variation of equatorial temperature for (a) equinox ($L_s = 355°$), (b) the 1977a global dust storm, and (c) the 1977b global dust storm. These sections all correspond to 180°W longitude.

in Fig. 14. The MGCM dust storm simulations have semidiurnal surface pressure oscillations at the two Viking Lander sites that are comparable in amplitude and phase with the observations and the LTM results. This agreement in $S_2(p)$ and the close correspondence between the observed and simulated T_{15} temperature variations in the summer (southern) hemisphere (Fig. 6) suggests that the thermotidal forcing due to aerosol has been reasonably well approximated in these dust storm simulations.

The effects of zonal-mean zonal wind and meridional (and vertical) variations of the zonal-mean temperature have been considered using zonal-mean fields obtained from MGCM integrations. As noted previously, the asymmetric MGCM tide response in Fig. 11 is due to the presence of relatively stronger westerlies in the northern hemisphere, as has been confirmed with LTM simulations using zonal-mean wind fields obtained from MGCM simulations. A similar asymmetry in the tidal response is evident in Fig. 16 of Wilson and Hamilton (1996) from an MGCM simulation for relatively clear solstitial conditions. We have also examined the LTM temperature response for zonal-mean conditions corresponding to the 1977a and 1977b global dust storms. A comparison of the LTM and MGCM dust storm simulations (not shown) indicates good agreement between the two models. Significantly, the pronounced amplification and poleward displacement of the $S_1(T_{15})$ maximum in the 1977a storm simulation relative to the 1977b solstice storm (Fig. 6) is evidently due to meridional gradients in the zonal mean wind (vorticity gradient) and is not predicted by classical tidal theory (Leovy and Zurek 1979), which is based on the assumption of a resting atmosphere.

Additional Calculations and Summary

The LTM calculations discussed above assumed uniformly mixed dust, so we have considered a number of alternative heating scenarios. These have included heating distributed predominantly at the altitude of peak T_{15} sensitivity, aerosol heating concentrated within the latitude range of the subsolar point, enhanced heating designed to simulate non-phase-shifted heat fluxes from the surface, and simulations designed to investigate the effect of a shift in phase of the convective heating with height. These variations generally had little effect on the qualitative nature of the tropical response. For sufficiently strong thermotidal forcing, the semidiurnal tide emerged as the dominant component of the T_{15} response, with temperature maxima consistently locked at roughly 0300 and 1500 LT. It was not possible to construct a plausible situation that yielded a large-amplitude tropical midday temperature maximum. It is important to emphasize that the observed tropical midday peak in IRTM T_{15} is such a consistent feature, present over a significant fraction of the martian year, that it is unreasonable to appeal to highly unusual dust distributions, idealized heating configurations, or circulation patterns that are unlikely to be sustained for any appreciable period. Indeed, the large variations in diurnal-mean tropical T_{15} over the Viking mission (Fig. 2) clearly reflect a range of dust loading conditions. It is also evident that any of a wide range of boundary-layer heating descriptions are unable to account for either the magnitude or the phase of the observed T_{15} variation. We conclude that the observed tropical diurnal variation in T_{15} during relatively clear periods is markedly inconsistent with the expected diurnal temperature variation of an atmospheric column averaged by the *nominal* 15-μm vertical weighting function.

4. REASSESSMENT OF THE IRTM 15-μm BRIGHTNESS TEMPERATURES

The strongly correlated diurnal variation of IRTM T_{15} and T_{20} discussed in Section 2 and the robust absence of a midday temperature maximum in simulated T_{15} (Section 3) together suggest that the IRTM 15-μm channel may have been more sensitive to surface radiance than indicated by the vertical weighting function associated with the nominal spectral response function. The IRTM instrument included a thermopile detector with a flat response from 3 to 30 μm, so that any stray radiation passed by the 15-μm channel multilayer interference filter would have resulted in contamination of the resulting T_{15} determination. We propose that the existence of a spectral leak in the 15-μm filter provides a simple and consistent explanation for the apparent presence of a significant surface temperature signal in the T_{15} data.

The Spectral Leak Hypothesis

In this section we examine the sensitivity of T_{15} to variations in the filter spectral response function. We created a set of trial filters by making different assumptions about the transmission in the vicinity of, and beyond the limits of, the passband of the nominal instrument filter. For any filter, we may calculate the total upwelling radiance associated with a specified vertical profile of surface and atmospheric temperature using high-resolution, frequency-resolved transmittances derived from a line-by-line radiation code. This procedure allows us to compare the diurnal variation of synthetic T_{15} with the observed diurnal variation.

We illustrate the consequences of a spectral leak at wavelengths well removed from the 15-μm CO_2 absorption band by using the two trial spectral response functions (A and B) shown in Fig. 17. The Mars CO_2 atmosphere is effectively transparent to radiation in the leakage ranges shown, so that the detector would see surface radiance with little attenuation. The resulting vertical weighting functions are little changed from that of the nominal instrument but for the development of a small but finite
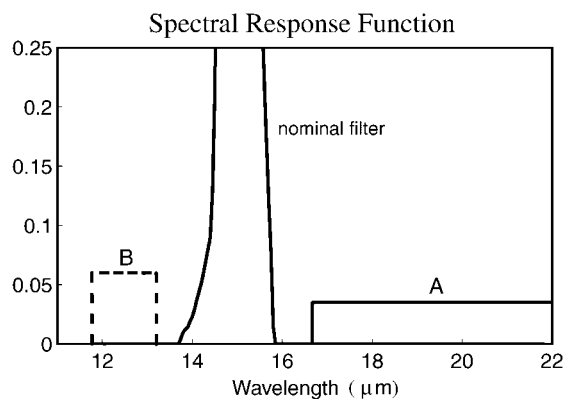

FIG. 17. The nominal IRTM spectral response function with trial filter leak region A (solid black) and filter leak region B (dashed line). The complete nominal IRTM spectral response is shown in Fig. 1 (top).
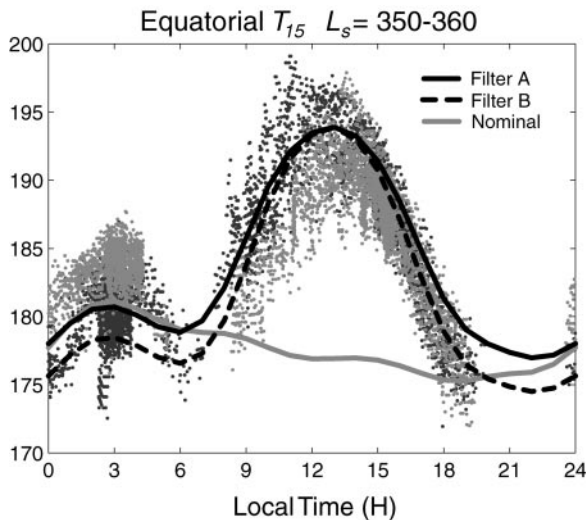
FIG. 18. A comparison of IRTM and synthetic T_{15} equatorial temperatures. The synthetic T_{15} temperatures are calculated from an MGCM simulation using the nominal and spectral leak instrument response functions shown in Fig. 17. The MGCM temperatures have been offset downward by 3 K for better display.

amplitude tail extending to relatively high pressures. The integrated effect of this tail provides a significant contribution from surface radiance while allowing little change in the contribution from the boundary layer. The observed lack of sensitivity of IRTM T_{15} to topographic elevations less than 13 km suggest that pressure-dependent contributions from boundary-layer radiance are insignificant relative to the surface in contributing to the midday temperature maximum.

We calculated synthetic T_{15} for each filter using atmospheric and surface temperatures from the MGCM simulation described in Section 3, corresponding to $L_s = 355°$. The diurnal variation of equatorial temperature for this simulation is shown in Fig. 16a. The MGCM yields surface temperatures in very close agreement with IRTM T_{20}. The comparison of the diurnal variation of synthetic T_{15} with the IRTM data is shown in Fig. 18. The synthetic T_{15} corresponding to leaky filters A and B closely agree with the IRTM data while the nominal filter yields a fairly modest diurnal variation with an early morning maximum, as discussed in Section 3. There is some sensitivity to the assumed location of the spectral leak. For example, the decrease in simulated T_{15} away from the midday peak is somewhat more rapid for filter B as a consequence of the increased temperature dependence of the Planck function at the shorter wavelengths (11.8–13.3 μm).

We have also considered spectral response functions that are somewhat broader than the nominal response. These yield weighting functions that give increased weight to radiance from both the surface and the lower scale height of atmosphere as a consequence of the finite atmospheric opacity at wavelengths in the vicinity of the edges of the nominal filter passband. As expected, these filters yield synthetic T_{15} with higher night temperatures and a less distinct midday maximum than the filters considered in Fig. 17. Moreover, these filters result in synthetic

T_{15} variations that are correlated with topography which is not supported by the data, as discussed in Section 2. The lack of sensitivity of IRTM T_{15} to topographic variations less than 13 km indicates that the majority of the spectral leak region is well removed from the 15-μm CO_2 absorption feature.

We have carried out his comparison procedure for other seasons as well, using temperatures from MGCM simulations appropriate for the corresponding season and dust loading. While the specification of the spectral leak is not unique, we do find that a fixed choice of filter with the leak sufficiently distinct from the 15-μm CO_2 band does provide a simple and consistent description of the observed IRTM T_{15} diurnal tropical temperature variation for all seasons.

Extracting Air Temperatures from the IRTM T_{15} Data

The preceding results suggest that we may estimate the radiance within the nominal filter spectral range, R_{15}, as the difference between R_{irtm}, the observed IRTM radiance, and R_{surf}, the radiance within the leak region. We attribute R_{surf} solely to the surface as the boundary layer evidently makes only a negligible contribution. The output from the IRTM thermopile detector was calibrated in the laboratory using black-body sources over a range of temperatures (Chase *et al.* 1978) so that the filter leak would have been implicily incorporated in the conversion of black-body temperature of radiance. Our calculations indicate that the effect of a spectral leak has negligible impact on the temperature–radiance dependence beyond a simple rescaling. Hence, for a given choice of filter leak scenario, we can calculate R_{irtm} from the IRTM T_{15} data. We chose to represent R_{surf} by using the observed T_{20} temperatures in the Planck function integrated over the spectral leakage range corresponding to filter B. The resulting radiance, R_{15}, is then converted back to an equivalent T_{15} temperature. This scheme returns the correct black-body temperature if the ground and air temperature are the same, and it is consistent with the laboratory calibration procedure.

It should be noted that the majority of the IRTM time-of-day coverage is provided by data from the Viking 1 Orbiter (VO1). The time-of-day coverage available from VO2 is insufficient to adequately establish the diurnal cycle at any point in the Mars year, and the limited longitudinal coverage precludes the construction of representative zonal averages. There is, therefore, insufficient VO2 data to provide an independent correction procedure for that instrument. The available VO2 temperatures are, however, consistent with those of VO1, so that a comparable spectral leak description of the 15-μm channel is evidently justified.

Of course, dust aerosol and water ice clouds could have some influence on the transmission and re-radiation of surface emission in the spectral leak region, depending on the exact wavelengths involved. For example, the 11- to 13-μm range is sensitive to the presence of water ice clouds (Curran *et al.* 1973), which appear to be particularly widespread during NH spring and summer (Clancy *et al.* 1996, Christensen 1998). Typical
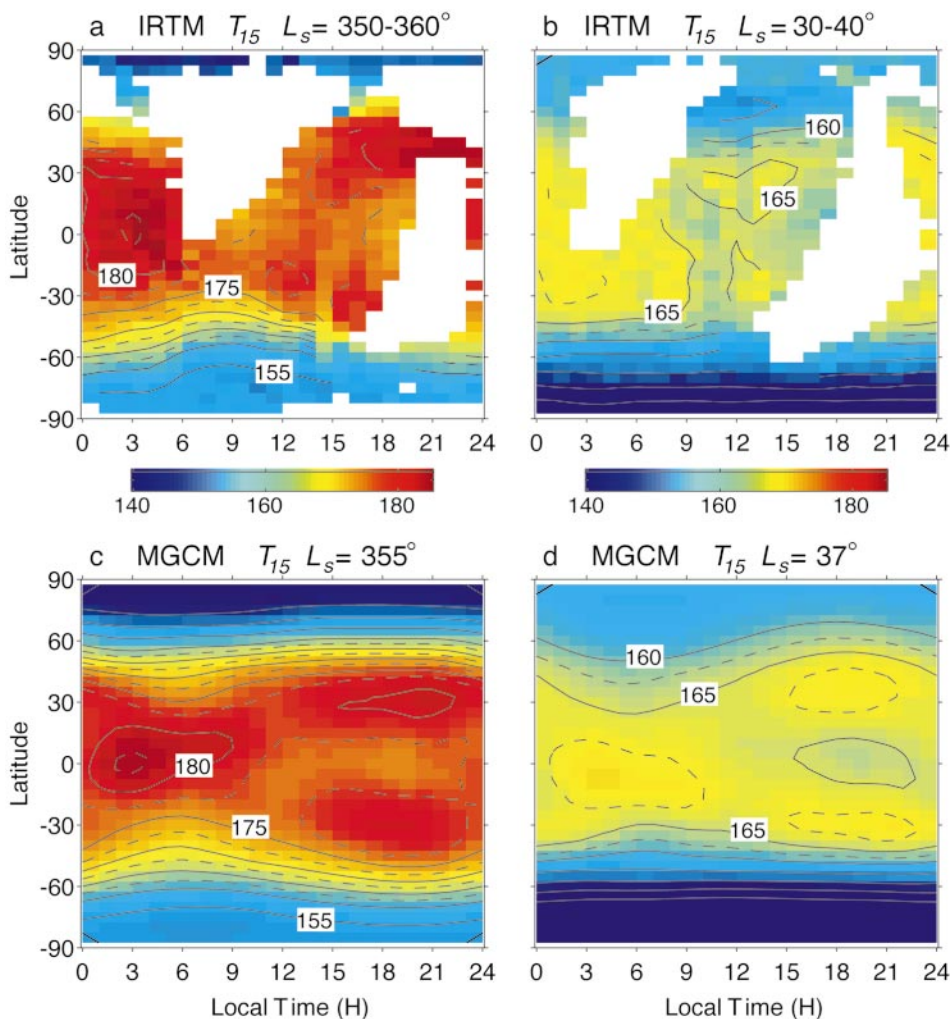
FIG. 19. Reprocessed IRTM T_{15} plotted as a function of latitude and local time for (a) $L_s = 350°-360°$ and (b) $L_s = 30°-40°$. Bottom panels show corresponding simulated T_{15} temperatures. Solid contour lines are in units of 10 K.

midday $T_{20}-T_{11}$ differences of 2–4 K have been observed during this season so that our use of T_{20} as the surface temperature would result in a modest overestimation of the correction of IRTM T_{15} when clouds are present. This could contribute spatial and temporal biases in the reprocessed temperatures corresponding to the variability of water ice clouds. We do, however, expect such effects to be relatively small. Similar considerations potentially apply in the presence of dust aerosol. In this case, T_{20} and, to a greater degree, T_9 can be distinctly less than T_7, which is least affected by dust or water ice clouds. The uncertainty in this case is of relatively little consequence since the temperature correction for surface radiance is smallest for dusty conditions.

Results of Reprocessing

Comparisons of reprocessed IRTM and MGCM T_{15} temperatures are shown in Fig. 19 for $L_s = 350°-360°$ and $L_s = 30°-40°$. The reprocessed IRTM T_{15} temperatures may also be contrasted with the original IRTM data shown in Fig. 4. The removal

of the hypothesized surface temperature contribution from the IRTM data allows the underlying atmospheric diurnal temperature variation to be revealed. In particular, the clear separation in phase between the tropical and midlatitude tidal response in quite evident in the reprocessed data for the $L_s = 350°-360°$ period, in good agreement with the MGCM simulation and the expectations of tidal theory. The location of the T_{15} temperature maxima agree fairly well with the MGCM simulation and with tide model predictions for moderate dust optical depths. A comparison (not shown) of reprocessed IRTM and simulated T_{15} temperatures for $L_s = 180°-190°$ (autumnal equinox) yields similarly good agreement, with a temperature pattern again showing a clear distinction between the tropical and extratropical tide responses.

The reprocessed IRTM T_{15} temperatures for $L_s = 30°-40°$ (Fig. 19) indicate a cooler atmosphere with evidently less diurnal variation than for the $L_s = 350°-360°$ period. The T_{15} temperatures for $L_s = 30°-40°$ are typical of the IRTM temperatures throughout the NH spring season except at high northern
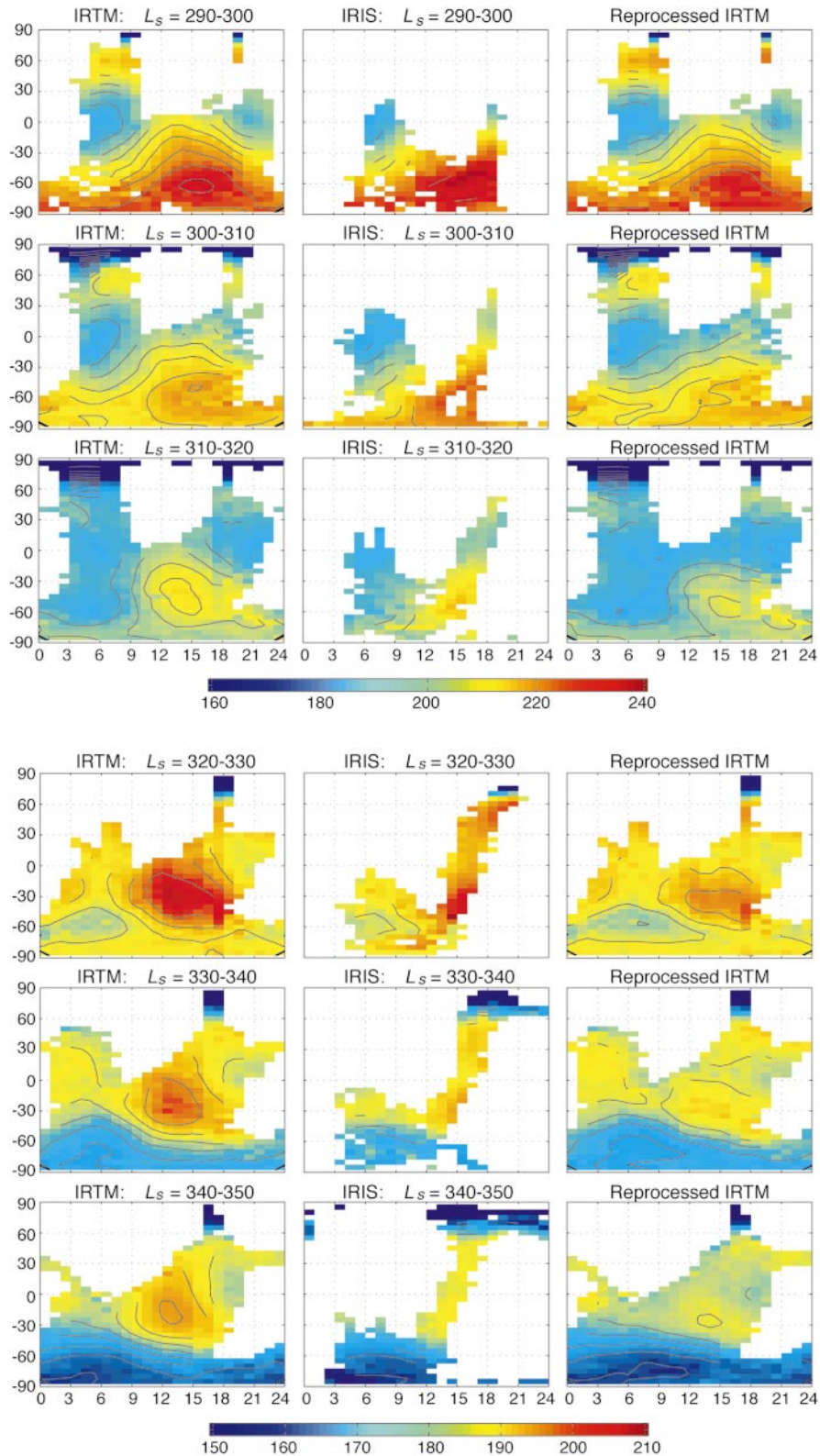
FIG. 20.   IRTM (left column) and Mariner 9 IRIS (center column) T_{15} temperatures as a function of latitude and local time for $L_s = 290°$–$350°$ in increments of $10°$. Reprocessed IRTM temperatures are shown in the right column. Note the change in the color scale for the bottom three rows. Contour intervals are 5 K.

latitudes, where there is a steady warming as the season progresses toward solstice. The relatively small diurnal and latitudinal temperature variation at tropical and middle latitudes in the spring season suggests a combination of rather low dust opacities and/or a relatively shallow dust distribution. The column opacity at the Viking Lander 1 site declined from 0.8 to roughly 0.6 in the $L_s = 360°$–$40°$ period (Colburn *et al.* 1989). This decline, in itself, does not fully explain the decrease in T_{15} tide amplitudes. Moreover, the amplitude of $S_2(p)$ at the VL1 site (Wilson and Hamilton 1996) remained constant during this period, suggesting that there was little variation in column-integrated thermotidal forcing. The diurnal temperature response at extratropical latitudes is vertically trapped and tends to reflect the vertical distribution of heating. We suggest that the reduction in the diurnal T_{15} variation is an indication that the height of the layer of significant aerosol heating fell below 25 km (0.5 mb) during this period.

During dusty periods, the enhanced emission from the relatively warm atmosphere is apparently sufficient to dominate surface emission so that the observed IRTM T_{15} temperatures are rather less subject to surface radiance bias. At the peak of the 1977b dust storm, surface temperatures were suppressed due to the heavy dust loading, and the correction to the IRTM T_{15} temperatures for the $L_s = 280°$–$290°$ period (Fig. 6b) is negligible. The maximum surface temperatures during the $L_s = 220°$–$225°$ period following the 1977a dust storm were in excess of 260 K in the southern subtropics and lead to modest changes in the IRTM T_{15} pattern shown in Fig. 6a. The qualitative change in the pattern is small, however, with the main consequence being a shift of the equatorial temperature maximum from ∼1400 to ∼1500 LT. This results in closer agreement with the MGCM simulation and is consistent with the dominant presence of $S_2(T_{15})$ as discussed in Section 3.

We have carried out this correction procedure for other seasons as well, using temperatures from MGCM simulations appropriate for the corresponding season and dust loading. In all cases, the diurnal variation of the reprocessed temperatures is in good agreement with that in the corresponding MGCM simulation. A detailed comparison of an MGCM simulation of the 1977 dust storm season with the Viking data is discussed in Part II of this study. It is significant that the reprocessing enables close agreement between the observed and simulated T_{15} to be obtained following each of the two global dust storms, while simultaneously matching the rise and decay of the semidiurnal surface pressure variation (which provides a measure of the thermal forcing). The simulated T_{15} fields in Figs. 6 and 19 were extracted from dusty and clear periods of this simulation.

5. COMPARISON BETWEEN IRTM AND IRIS T_{15} TEMPERATURES

In addition to the IRTM T_{15} observations, orbiter-based infrared measurements of martian atmospheric temperatures are available from the Mariner 9 IRIS data set. This data set consists

of over 21000 thermal emission spectra which provided continuous observations of Mars during the primary mission covering the period $L_s = 293°$–$352°$ in 1971–1972. After $L_s = 352°$, only an additional 64 spectra were recorded through NH summer ($L_s = 97°$). The spectral data were obtained in the range 200 to 2000 cm^{-1} (5–50 μm) with 2.4 cm^{-1} resolution (Hanel *et al.* 1972a) enabling us to synthesize an equivalent set of T_{15} and T_{20} observations (hereafter IRIS T_{15} and T_{20}) by convolving the IRIS data with the corresponding IRTM filter response functions. This procedure allows for a direct comparison of IRIS and IRTM results. As with the IRTM data, we have restricted our attention to spectra with emission angles less than 60°.

Mariner 9 arrived at Mars well after the onset ($L_s = 264°$) of the global dust storm that is regarded as the most extensive storm on record (Martin and Zurek 1993). The atmosphere was still very dusty during the early part of the primary mission, as was evident in the visual observations and the elevated temperatures. By $L_s = 319°$ the dust began to dissipate, and the clearing was well advanced by $L_s = 340°$. This behavior is well illustrated in the evolution of subtropical IRIS temperatures as presented by Conrath (1975). Figure 20 shows a comparison of IRIS and IRTM T_{15} temperatures from $L_s = 290°$ to $L_s = 350°$ in increments of 10° of areocentric longitude. The reprocessed IRTM temperatures are also shown. The similarity of temperature patterns through $L_s = 310°$ suggests comparable atmospheric heating due to aerosol. Both data sets suggest late-afternoon temperature maxima at high southern latitudes and distinct temperature minima occurring in the tropics at 0400–0600 LT. The role of aerosol heating in forcing the extratropical tide evident in the IRIS data has been discussed by Pirraglia and Conrath (1974) and Leovy and Zurek (1979). Although the data coverage during the Mariner 9 mission is rather sparse, the available data are not inconsistent with the presence of a semidiurnal temperature variation in the tropics. Again, the MGCM simulation of the 1977b global dust storm (Fig. 6) provides context for comparing the IRTM and IRIS T_{15} temperature patterns. Afternoon IRIS tropical temperatures (1500–1500 LT) remain warmer than morning temperatures (∼0600 LT) for much of the late NH winter period ($L_s = 290°$–$340°$), which is consistent with the presence of a non-negligible (but decaying) semidiurnal tide (see Fig. 16). The rather incomplete time-of-day IRIS coverage clearly makes the data interpretation somewhat uncertain and highlights the utility of the tidal modeling discussed in Section 3.

Significantly, there is an increasing divergence in the pattern of diurnal tropical temperature variation as the season progresses toward spring and the atmospheric temperatures decline. Difference maps (not shown) indicate the emergence of the surface temperature bias in the IRTM data with the difference rising to over 10 K at the edge of overlapping coverage nearest to equatorial noon. The IRIS data for $L_s = 320°$–$350°$ consistently indicate a relatively flat tropical temperature variation with local time in the mid-afternoon hours, in contrast to the marked decrease in temperature away from local noon in the IRTM data set. The IRIS temperatures suggest the presence of two late

afternoon extratropical temperature maxima, which agrees with the simulated patterns in Fig. 19 and with the reprocessed IRTM temperatures.

Santee and Crisp (1993) used IRIS spectra to simultaneously retrieve temperature profiles and dust optical depth for the $L_s = 343°$–$348°$ period. Santee and Crisp show a latitude vs local time presentation of the retrieved temperatures at the 0.5-mb level which generally agrees with the IRIS T_{15} temperatures presented here. It should be noted, however, that the contours in Figs. 11 and 12d of Santee and Crisp (1993) have been extended into regions with poor or no data coverage. For example, the indicated closing off of the late-afternoon 0.5-mb temperature contours in the southern extratropics is a consequence of the technique used to extrapolate the data.

Haberle et al. (1993) compared a 1400 LT, 0200 LT difference height–latitude section from the NASA Ames Mars GCM with that derived by Santee and Crisp (1993). The Ames MGCM results (Fig. 17 in Haberle et al.) indicate the presence of a vertically propagating thermal tide in the tropics, with the 0.5-mb temperature maximum occurring at ~0200 as expected from the results in this paper. By contrast, Fig. 12c in Santee and Crisp (Fig. 17 in Haberle et al.) indicates that afternoon (1400 LT) temperatures are warmer than the morning (0200 LT) temperatures at all heights. Our examination of the IRIS data shows that the plotted 0200 LT tropical temperatures were based on spectra with emission angles greater than 60°. These spectra yielded anomalously cold T_{20} and T_{15} temperatures with very marked dependence on emission angle, strongly indicating that these data may not reliably represent surface and 0.5-mb temperatures. As a consequence, it would appear that there are no reliable morning data for the tropics with which to construct such a figure. We suggest that the negative meridional temperature gradient at tropical latitudes in the 0200 LT figure (Fig. 12b of Santee and Crisp 1993) is an artifact of the erroneous data corresponding to high emission angles. We conclude that the IRIS data are not inconsistent with the diurnal temperature variations suggested by tide modeling. This discussion highlights the need for care when interpreting spacecraft data.

It is of interest to extend this comparison through the full course of the Mariner 9 mission. As noted above, this is made difficult by the very sparse IRIS coverage after $L_s = 352°$. The IRIS tropical temperatures for $L_s = 4°$ show a continued cooling as the season progresses into spring, and, at ~178 K, they are comparable (within 3 K) to corresponding IRTM morning temperatures. The midday IRTM temperatures, however, exceed 190 K, so that this difference (>10 K) is consistent with the emerging midday differences noted during late winter. A comparison of the IRIS and IRTM T_{15} temperatures for the $L_s = 42°$–$55°$ period has been presented and discussed by Richardson (1998). Again, there is very close agreement between IRTM and IRIS observations (~168 K) for latitudes and local times well removed from tropical noon. The largest differences (~10 K) occur for the tropical temperatures closet to noon (0930–0945), as has been shown in a point-by-point comparison given in Table 1

of Richardson (1998). These differences are consistent with the proposed surface temperature bias in the IRTM data, and the reprocessing of IRTM T_{15} removes these differences.

Finally, we consider the comparison of IRTM and IRIS temperatures for $L_s = 95°$–$98°$. In particular, the three IRIS T_{15} observations (167 K) around 0600 LT at 19°–22°N are within a degree or two of corresponding (in latitude, local time, and longitude) IRTM T_{15} observations. By contrast, there is again a roughly 10-K difference in IRTM and IRIS T_{15} (180 K vs 170 K) temperatures for the observations at 1600 LT, as was noted by Kieffer et al. (1976a). This is comparable to the difference between IRTM and simulated T_{15} at this local time, as indicated in Fig. 5.

Apart from differences in the behavior of temperatures near the subsolar point, the decline in temperature during the entire dust storm decay period is quite similar during the Mariner 9 and Viking missions. The pattern of increasing temperature differences in the vicinity of tropical midday is consistent with our suggestion of a surface temperature bias in the IRTM data. The close correspondence between IRIS and reprocessed IRTM temperatures evidently extends into the following spring season, so we conclude that differences between IRIS and IRTM temperatures are largely attributable to the filter leak.

Mars Global Surveyor TES Results

Currently available temperature retrievals from the MGS TES instrument (orbits 20–36, $L_s = 198°$–$208°$) indicate temperature variability consistent with the simulated thermal tides and show no evidence for the presence of a midday tropical temperature maximum. The coverage in local time in the tropics, however, is limited to morning and to late afternoon. In the future, TES results will likely be more useful in this regard as the orbiter eases into a 0200/1400 LT mapping orbit. We anticipate that synthesized T_{15} TES observations will indicate tropical 0200 LT temperatures comparable to, if not slightly higher than, 1400 LT temperatures for low-dust conditions when the semidiurnal tide contribution is not significant.

6. MARS CLIMATE

A significant result of our identification of a surface radiance bias in the IRTM T_{15} data is an improved definition of the seasonal cycle of martian atmosphere temperatures during the Viking mission. In this section we present revised IRTM temperatures and make comparisons with other temperature observations. The revised data are found to have important implications for our understanding of interannual climate variability.

The latitudinal and seasonal distribution of the reprocessed, diurnally averaged IRTM T_{15} temperatures is shown in Fig. 21, which may be contrasted with the original T_{15} data shown in Fig. 2. Again, it should be noted that the available data have simply been zonally averaged so that the diurnal average is poorly represented in some instances due to limited diurnal coverage. For example, diurnally averaged tropical temperatures for the
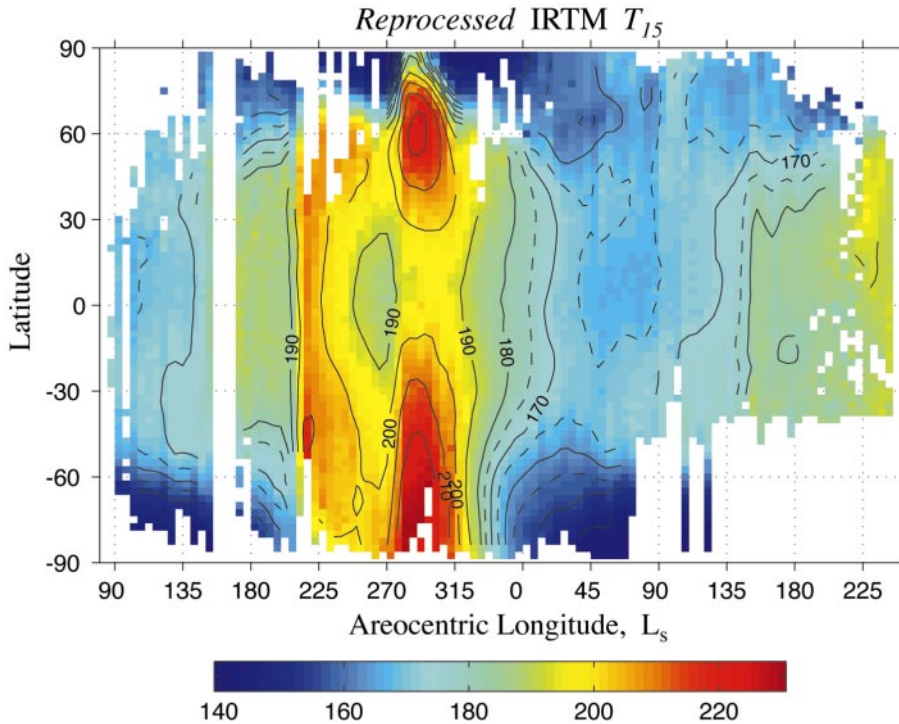
FIG. 21. Latitudinal and seasonal distribution of reprocessed IRTM T_{15} temperature. Solid contour lines are in units of 10 K. The temperatures represent diurnal averages to the extent possible.

period following the 1977b global dust storm have a cold bias due to the pattern of the local time coverage which emphasizes the cold phases of the semidiurnal temperature variation (see Fig. 6). A comparison of "diurnally averaged" temperatures computed from the MGCM 1977b dust storm simulation (Fig. 6) using the full and observed local time coverage suggests that the tropical temperatures in Fig. 21 are 4 to 8 K colder than the "true" diurnal average. Similarly, the estimate of the diurnal average tropical temperature following the 1977a dust storm has a warm bias as suggested by Fig. 6. The diurnal variation of corrected T_{15} is relatively less in non-dusty seasons so that the estimate of the diurnal average should be less sensitive to limited diurnal sampling. By contrast, the estimates of diurnally averaged, uncorrected IRTM T_{15} temperatures (Fig. 2) during NH spring and summer have a warm bias due to disproportionate midday coverage (see Fig. 4) when the surface temperature effect is most prominent. We anticipate that, in general, guidance from MGCM simulations will allow for an improved accounting of limited diurnal coverage in formulating diurnal average temperatures.

The reprocessed T_{15} in Fig. 21 tend to be somewhat cooler than the original data in Fig. 2, particularly during the NH spring and summer seasons when the contrast between atmosphere and surface temperatures is greatest. The revised temperatures are ∼10 K cooler at northern midlatitudes as a consequence of the strong surface temperature bias near the subsolar point. There is also a more pronounced cooling of equatorial and southern

hemisphere temperatures during the decaying phase of the 1977a dust storm.

There is a significant qualitative change in the latitudinal structure of the diurnal average temperatures as a result of the reprocessing. The original IRTM T_{15} temperatures (Fig. 2) indicate a distinct cross-equatorial temperature gradient during the NH spring and summer solstice seasons as the temperature maximum tends to migrate with the subsolar latitude. By contrast, the revised T_{15} temperatures (Fig. 21) show a relatively symmetric meridional distribution in the vicinity of the equator throughout the annual cycle. This result is consistent with MGCM simulations of zonal-mean temperatures (Haberle *et al.* 1993, Wilson and Hamilton 1996, Wilson 1997). Recent MGS TES (Conrath *et al.* 2000) temperature observations also indicate this symmetry. A latitude–height cross section of retrieved IRIS temperatures for the $L_s = 42°$–55° period (Leovy 1982) indicates a flat meridional temperature variation throughout the tropical and middle latitudes above 2 mb. The IRIS 0.5-mb and T_{15} temperatures are ∼168 K, in reasonable agreement with Fig. 19. The corrected IRTM T_{15} temperatures corresponding to the T_{15} and T_{20} observations shown in Fig. 9 ($L_s = 53°$, 1130 LT) are uniform with latitude over the range 30°S to 30°N.

A cross-equatorial temperature gradient well removed from the surface is inconsistent with dynamical considerations as the thermal wind relation provides a strong constraint on the atmospheric thermal structure (Schneider 1983). Thus, hemispherically asymmetric thermal forcing results in dynamical heating
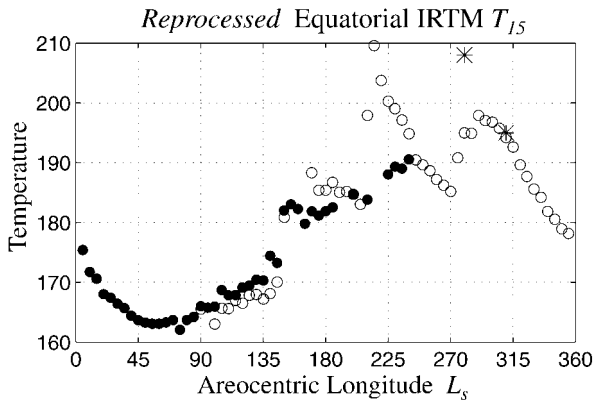
FIG. 22. Seasonal evolution of reprocessed IRTM T_{15} equatorial temperature. The asterisks indicate estimates of equatorial temperature based on the 1977b dust storm simulation in Fig. 6.

(due to adiabatic descent) in the winter hemisphere which balances the net radiative heating in the summer hemisphere, yielding a symmetric temperature distribution. For increasing thermal forcing, theory (Schneider 1983) and model simulations (Haberle *et al.* 1993, Wilson and Hamilton 1996, Wilson 1997) indicate a deepening relative temperature minimum at the equator, as seen in Figs. 6 and 21, during dusty periods.

The revised equatorial temperatures are shown in Fig. 22. The asterisks indicate estimates of the true diurnal average equatorial temperature based on the 1977b dust storm simulation (see Fig. 6), as discussed above. The rate of decline of diurnal average temperature following each of the two 1977 dust storms is comparable, and is distinctly more rapid than is indicated in the original IRTM data. The semidiurnal temperature variation derived from reprocessed T_{15} data following the two dust storms shows a rapid decline in amplitude in a manner that is consistent with the observed rapid decline in $S_2(p)$ amplitude at the VL1 site (Wilson and Hamilton 1996). As discussed in Section 5, the temperature decline following the 1977b storm is comparable to the decay of IRIS temperatures following the 1971 global dust storm. This would suggest that the general evolution of the aerosol distribution was rather similar following the two solstitial dust storms. Evidently, for each case, the atmosphere clears at a rapid rate and loses much of it memory of the global dust storm in the preceding season.

Interannual Variability of Aphelion Season Temperatures

Figures 21 and 22 suggest that there is relatively little difference in temperature during the NH spring and summer seasons for the two years shown. Note that the limited data in the third martian year is not shown due to the poor diurnal coverage. Richardson (1998) showed that when IRTM T_{15} temperatures for NH spring and summer are compared with consideration of local time and latitude, the observations are found to closely correspond among all three years, suggesting there is little interannual temperature variation in this season. This is also con-

sistent with the finding that IRTM and IRIS temperatures for the $L_s = 42°$–$55°$ period are comparable. Moreover, the amplitudes and phases of the diurnal and semidiurnal surface pressure tides at the VL1 site (Wilson and Hamilton 1996) are virtually identical for 4 years in this season, further suggesting a highly repeatable climate.

Earth-based microwave observations (Clancy *et al.* 1990, 1996) have provided a multi-year record of disk-averaged temperature profiles of the martian atmosphere. The comparison of IRTM and microwave observations requires proper spatial averaging of the IRTM values to account for the fact that whole-disk microwave observations primarily weight atmospheric temperatures near the subsolar point. The 15–20 K difference resulting from comparison of 0.5-mb microwave observations and suitably averaged IRTM T_{15} values during non-dust-storm periods had been interpreted as evidence for a relatively warm and dusty climate during the Viking mission that preceded a shift to a cooler and clearer current climate in more recent years (Clancy *et al.* 1990, 1996). However, Richardson (1998) showed that simultaneous IRTM T_{15} and microwave observations from May 1980 exhibited the same 15–20 K offset and concluded that the difference between the two data sets is a result of a bias in one or both of the observational systems. Significantly, the subsolar-point temperatures are the most strongly affected by the surface temperature biasing of T_{15}. We find that suitably averaged, corrected T_{15} temperatures fall by roughly 10 K during relatively clear sky conditions, which suggests that the proposed T_{15} correction can explain at least half to two-thirds of the bias. Note that it is unlikely that the remaining difference represents evidence of a climate change for the same reasons discussed by Richardson (1998). Further study with MGCM simulations is underway to better understand how to compare disk-averaged observations to spatially (and temporally) resolved model and spacecraft data. The close correspondence between MGS TES and microwave temperatures at 0.3-mb (Clancy *et al.* 2000) supports the utility of the microwave data, and the multi-year record of microwave observations provides further evidence that the aphelion season is one of little variability.

An interesting aspect of the IRTM T_{15} record are the abrupt temperature increases of ∼10 K at $L_s ∼ 145°$ in 1976 and in 1978 that are evident in Figs. 21 and 22. The temperature jumps appear simultaneously at all latitudes from 40°S to 40°N and occur at the season when the rapid variations in the amplitudes and phases of the diurnal and semidiurnal tides are present in the Viking Lander 1 surface pressure record (Tillman 1988, Wilson and Hamilton 1996). These "Tillman transients" are most likely a reflection of changes in the longitudinal interference pattern between the sun-synchronous thermal tides and eastward-propagating, resonantly enhanced Kelvin modes (Wilson and Hamilton 1996). MGCM simulations indicate that the VL1 tides are particularly sensitive to variations in thermotidal forcing in this season. The temperature jumps are not accompanied by significant opacity changes (Colburn *et al.* 1989) at either of the two Viking Lander sites. The IR opacity determinations by Martin

and Richardson (1993) do suggest modest opacity changes at this time; however, these estimates are partly based on the original T_{15} data and may require recalculation.

Retrieved Temperature Profiles

Viking and Pathfinder lander entry acceleration measurements (Sieff and Kirk 1977, Schofield *et al.* 1997) and Viking orbiter radio occultation data (Lindal *et al.* 1979) have yielded instantaneous temperature profiles with relatively high vertical resolution. We now consider the comparison of these profiles with the reprocessed IRTM temperatures. The limited Viking mission radio occultation data appear to agree with the reprocessed IRTM data. Specifically, three temperature profiles acquired during the second Viking year (Lindal *et al.* 1979) around $L_s = 75°$ at 1600 LT in the vicinity of the VL1 site show air temperatures falling more rapidly with altitude than either of the two Lander entry profiles, decreasing to ∼170 K at 20 km. By contrast, IRTM T_{15} observations for the corresponding season, location, and local time consistently indicate T_{15} temperatures of ∼180 K while the corrected IRTM temperatures are ∼166 K, which is roughly consistent with the occultation measurement. These temperatures are comparable to the Mariner 9 IRIS temperatures (∼168 K) for the $L_s = 42°$–55° and $L_s = 98°$ periods.

The Mars Pathfinder entry temperature profile (Schofield *et al.* 1997) at $L_s = 142°$ corresponds to a T_{15} temperature of ∼183 K, which is in rough agreement with IRTM temperatures for late NH summer. Recall that IRTM temperatures show a rapid 10 K increase around this season ($L_s = 140°$–150°) in each of two years for which there is IRTM data (Fig. 22). The local time of entry (0330 LT) was such that the IRTM T_{15} would be largely unaffected by surface emission.

IRTM T_{15} temperatures in the vicinity of VL1 (22°N at 1613 LT) range from 175 to 180 K and are in reasonable correspondence with the effective T_{15} value of 183 K derived from the VL1 entry profile. Similarly, IRTM temperatures in the vicinity of VL2 (48°N at 0906 LT) range from 173 to 182 K, in rough agreement with the VL2 T_{15} estimate of 183 K. Pre-dawn (0600 LT) IRTM T_{15} air temperatures were 165–172 K at both lander sites. The entry latitudes and local times are such that the surface emission signal (e.g., Fig. 5) brings the corrected IRTM T_{15} down by ∼10 K relative to these entry profiles. There is no clear indication of either sol-to-sol or interannual variability in this season for the two years for which data is available which might explain this difference. This inconsistency between the reprocessed IRTM T_{15} temperatures and the two Viking entry profiles represents the only discrepancy between the reprocessed data and any other data set or theoretical model. This issue will require further investigation into the representativeness of single-column observations.

Water-Ice Clouds

The downward revision of Viking-period 0.5-mb temperatures for NH spring and summer implies a lower atmospheric water vapor saturation level than had been indicated by the measured IRTM temperatures. The potential significance of a lower saturation level has been discussed by Clancy *et al.* (1996) in the context of the relatively cooler microwave temperatures. Hubble Space Telescope images (Clancy *et al.* 1996, James *et al.* 1996), the analysis of IRTM T_{11} and T_{20} data (Tamppari *et al.* 2000, Toigo and Richardson 2000), and the analysis of MGS TES spectra (Pearl *et al.* 1999) have suggested that an extensive tropical water ice cloud belt may be a prominent feature of the martian atmosphere during the aphelion season. Based on a comparison of IRTM T_{11} and convolved IRIS spectra, Christensen (1998) has suggested that water-ice hazes of similar optical depth may have occurred in this season during the Mariner 9 and Viking missions. This would be consistent with little interannual variability in atmospheric temperatures in this season.

The tide results presented in this paper have implications for the formation of water-ice clouds which may be sensitive to the diurnal variation in atmospheric temperature (e.g., Colburn *et al.* 1989, Michelangeli *et al.* 1993). At tropical latitudes, the variation in height of the phasing of the temperature maximum will affect the diurnal cycle of cloud growth and decay. For example, a tendency for tropical clouds to dissipate in late morning (Colburn *et al.* 1989) might suggest that they are forming at relatively low altitudes, which would be consistent with the lower temperatures implied by our revision of IRTM temperatures, and with the results of Clancy *et al.* (1996). Figure 16a indicates that a transition from maximum temperatures at midday to morning hours may occur at at ∼1–2 mb (∼15 km). At extratropical latitudes, the maximum temperatures occur during afternoon at all pressure levels; however, for relatively clear conditions, the diurnal temperature variation is fairly small (much smaller than indicated by the uncorrected IRTM observation), and consequently, there may be little diurnal variation in cloudiness, depending on the height of formation. Of course, ground fogs would be expected to show a pronounced diurnal cycle. We speculate that the temperature jumps in Fig. 21 may indicate a discrete increase in the depth of the layer of dust heating associated with a seasonally dependent dust/water ice interaction (Rodin *et al.* 1999). Further analysis of IRTM T_{11} and T_{20} data (Tamppari *et al.* 2000) and MGS TES spectra may offer insight into the presence and behavior of water-ice clouds in this season.

7. SUMMARY

This study began as a project to compare the simulation of thermal tides in the GFDL Mars GCM with those present in the IRTM T_{15} data set. We found that for the particularly dusty periods corresponding to the two 1977 global dust storms, the pattern of variation in latitude and local time of simulated T_{15} is very consistent with the IRTM T_{15} data. By contrast, simulations employing weak to moderate dust column opacities consistently yield a tropical T_{15} diurnal variation significantly in disagreement with the much stronger diurnal variation indicated by the

IRTM observations during relatively clear periods. The observed diurnal and longitudinal T_{15} variations are closely correlated with surface temperature variations, suggesting the possibility that the IRTM T_{15} temperatures were biased by surface emission. A wide range of calculations with a Linear Tidal Model were carried out to demonstrate that the observed strong midday T_{15} maximum is robustly inconsistent with the expected atmospheric response to any reasonable diurnal forcing. Rather, we propose that the disagreement between MGCM tidal results and IRTM T_{15} data is most plausibly accounted for by the presence of a leak in the 15-μm channel filter which allowed surface radiation to contaminate the measured radiances. The examination of IRTM T_{15} and surface temperatures as a function of surface elevation suggests that the leak lies at wavelengths largely unaffected by CO_2 absorption, which allows for a relatively simple procedure for removing the surface influence from the observed radiances. While variations in surface emissivity, atmospheric aerosol, and water-ice opacity effects can introduce errors into the correction process, such errors will likely be small relative to both the magnitude of the correction near the subsolar point ($\sim$15 K) and the inherent variability of the T_{15} data.

An important result of the identification of the surface temperature bias is that good agreement between MGCM simulations and the IRTM data can be achieved. We also found that MGCM simulations were additionally consistent with the Viking Lander semidiurnal surface pressure observations, which may serve as an independent constraint on globally integrated aerosol heating (Leovy and Zurek 1979). This result provides increased confidence in the fidelity of the representation of the Mars atmosphere by general circulation models. The MGCM simulations demonstrate the potential for extrapolating temperature observations and in doing so, providing insight into the underlying circulation and dynamics.

A major consequence of this work is the improved definition of the diurnal, latitudinal, and seasonal variation of atmosphere temperatures during the Viking mission. The surface bias is most pronounced during relatively clear periods ($L_s = 320°$–$180°$) so that corrected tropical midday T_{15} temperatures are as much as 15 K colder than previously indicated. The revised global mean temperatures in the aphelion season (centered about $L_s \sim 70°$) are now roughly comparable to those indicated by the Mariner 9 IRIS observations and ground-based microwave profiling (Clancy *et al.* 1996). This general agreement is consistent with the finding that 3 years of IRTM temperatures provide no evidence for interannual temperature variability in this season (Richardson 1998). The similarity of 4 years of VL1 surface pressure tidal oscillations (Wilson and Hamilton 1996) further supports this suggestion.

Our comparison of IRIS and IRTM T_{15} temperatures indicates that there is a comparable decay in atmospheric temperatures following the solstitial global dust storms of 1971 and 1977. Evidently the atmosphere clears at a rapid rate and loses memory of the dust storms in the previous season. The revised temperatures and thermal tides indicate a relatively cold atmosphere during

the aphelion season that, at least at the 0.5-mb level, is also evidently relatively clear. It may be that the dust distribution is vertically confined, perhaps by the radiative/dynamical effects of water ice condensation occurring at relatively low altitudes due to cool temperatures (Rodin *et al.* 1999). The two years of IRTM observations suggest a rapid transition from the aphelion season temperatures. Further observations and analysis will be required before a completely consistent picture of the behavior of martian mid-level air temperatures emerges. It is anticipated that MGCMs will play an important role in synthesizing the current and upcoming stream of spacecraft data.

APPENDIX: CLASSICAL TIDAL THEORY

Tidal oscillations are global-scale inertia-gravity waves whose ability to propagate vertically depends on whether the forcing frequency, σ, is larger than the effective Coriolis frequency, $f_{\text{eff}}(f = 2\Omega \sin \phi$, where Ω is the planetary rotation rate and ϕ is the latitude). For the diurnal components in an atmosphere at rest, the transition from vertically propagating behavior to vertically trapped behavior takes place at $\phi_{\text{eff}} = 30°$ latitude. For semidiurnal forcing, σ is greater than f at all latitudes so that the semidiurnal tides are vertically propagating everywhere. Vertically trapped modes are localized in the immediate region of thermal forcing, whereas the amplitude of a propagating mode can grow with height away from the level of forcing. This latter behavior is a consequence of conservation of energy in an atmosphere where density decreases with height. High-frequency oscillations (motions faster than the local pendulum day) are characterized by divergent, cross-isobaric flow while lower frequency oscillations tend to be quasi-nondivergent, with flow roughly parallel to the isobars so that the motion is quasi-geostrophic. The longer forcing periods provide sufficient time for geostrophic balance to be established, and the resulting vertical motion is relatively weak. The development of vertical velocity provides the atmosphere with a means to balance thermal forcing by adiabatic heating or cooling, an effect that need not be confined to the region of forcing. Hence the dynamic response of the atmosphere can cause temperatures at a given level to deviate substantially from what would be expected on the basis of radiative effects alone.

In the case of an atmosphere at rest, the horizontal structure of these inertia-gravity waves is described by the Laplace tidal equation with the well-known Hough function solutions (e.g., Chapman and Lindzen 1970). Each Hough function solution may be identified with a vertical structure function. The atmospheric response is determined by the projection of the thermotidal forcing onto these modes. For diurnal forcing, the Hough functions cluster into two groups, describing modes that are relatively confined to tropical latitudes ($\phi_{\text{eff}} < 30°$) and modes that tend to be confined to extratropical and polar latitudes. The modes in the former set are vertically propagating while the latter are vertically trapped. The meridionally broadest equatorial mode has a vertical wavelength of roughly 33 km, while higher meridional modes have shorter vertical wavelengths.

The meridionally broadest semidiurnal Hough function, which most closely matches the latitude distribution of any reasonable thermotidal forcing, has a vertical wavelength of roughly 200 km. The broad meridional scale and deep vertical structure of this semidiurnal tidal mode allows the semidiurnal surface pressure oscillation, $S_2(p)$, to respond efficiently to aerosol heating. This property is the basis for the close relationship between globally averaged aerosol optical depth and the amplitude of $S_2(p)$ indicated by the Viking Lander 1 surface pressure record (Zurek and Leovy 1981).

ACKNOWLEDGMENTS

REFERENCES

Banfield, D., A. D. Toigo, A. P. Ingersoll, and D. A. Paige 1996. Martian weather correlation length scales. *Icarus* **119**, 130–143.

Chapman, S., and R. S. Lindzen 1970. *Atmospheric Tides*. Reidel, Pordrecht.

Chase, S. C., J. L. Engle, H. W. Eyerly, H. H. Kieffer, F. D. Palluconi, and D. Schofield 1978. Viking infrared thermal mapper. *Appl. Opt.* **17**, 1243–1251.

Christensen, P. R. 1998. Variations in martian surface composition and cloud occurrence determined from thermal infrared spectroscopy: Analysis of Viking and Mariner 9 data. *J. Geophys. Res.* **103**, 1733–1746.

Christensen, P. R., and H. J. Moore 1992. The martian surface layer. In *Mars* (H. H. Kieffer, B. M. Jakosky, C. W. Snyder, and M. S. Matthews, Eds.), pp. 686–729. Univ. of Arizona Press, Tuscon.

Clancy, R. T., and S. W. Lee 1991. A new look at dust and clouds in the Mars atmosphere: Analysis of emission-phase-function sequences from global Viking IRTM observations. *Icarus* **93**, 135–158.

Clancy, R. T., A. W. Grossman, M. J. Wolff, P. B. James, D. J. Rudy, Y. N. Billawala, B. J. Sandor, S. W. Lee., and D. O. Muhleman 1996. Water vapor saturation at low altitudes around Mars aphelion: A key to Mars climate? *Icarus* **122**, 36–62.

Clancy, R. T., D. O. Muhleman, and G. L. Berge 1990. Global changes in the 0–70 km thermal structure of the Mars atmosphere derived from 1975 to 1989 microwave CO spectra. *J. Geophys. Res.* **95**, 14,543–14,554.

Clancy, R. T., B. J. Sandor, M. J. Wolff, P. R. Christensen, M. D. Smith, J. C. Pearl, B. J. Conrath, and R. J. Wilson 2000. An intercomparison of ground-based millimeter, MGS TES, and Viking atmospheric temperature measurements: Seasonal and interannual variability of temperatures and dust loading in the global Mars atmosphere. *J. Geophys. Res.* **105**, 9553–9571.

Colburn, D. J., J. Pollack, and R. Haberle 1989. Diurnal variations in optical depth at Mars. *Icarus* **79**, 159–189.

Conrath, B. J. 1975. Thermal structure of the martian atmosphere during the dissipation of the dust storm of 1971. *Icarus* **24**, 36–46.

Conrath, B. J., R. Curran, R. Hanel, V. Kunde, W. Maguire, J. Pearl, J. Pirraglia, J. Welker, and T. Burke 1973. Atmospheric and surface properties of Mars obtained by infrared spectroscopy on Mariner 9. *J. Geophys. Res.* **78**, 4267–4278.

Conrath, B. J., J. C. Pearl, M. D. Smith, D. Banfield, and P. R. Christensen 2000. Observations of the thermal structure and dynamics of the martian atmosphere. *J. Geophys. Res.* **105**, 9509–9519 (April 25, 2000).

Curran, R. J., B. J. Conrath, R. A. Hanel, V. G. Kunde, and J. C. Pearl 1973. Mars: Mariner 9 spectroscopic evidence for H_2O ice clouds. *Science* **182**, 381–383.

Gierasch, P. J., and R. M. Goody 1968. A study of the thermal and dynamical structure of the martian lower atmosphere. *Planet. Space Sci.* **16**, 615–646.

Haberle, R. M., J. B. Pollack, J. R. Barnes, R. W. Zurek, C. B. Leovy, J. R. Murphy, H. Lee, and J. Schaeffer 1993. Mars atmospheric dynamics as simulated by the NASA Ames General Circulation Model 1. The zonal mean circulation. *J. Geophys. Res.* **98**, 3093–3123.

Hanel, R. A., B. J. Conrath, W. A. Hovis, V. G. Kunde, P. D. Lowman, J. C. Pearl, C. Prabhakara, and G. Schlachman 1972a. Infrared spectroscopy experiment on the Mariner 9 mission: Preliminary results. *Science* **175**, 305–308.

Hanel, R., B. Conrath, W. Hovis, V. Kunde, P. Lowman, W. Maguire, J. Pearl, J. Pirraglia, C. Prabhakara, and B. Schlachman 1972b. Investigation of the martian environment by infrared spectroscopy on Mariner 9. *Icarus* **17**, 423–442.

Hess, S. L, R. M. Henry, C. B. Leovy, J. A. Ryan, and J. E. Tillman 1977. Meteorological results from the surface of Mars: Viking 1 and 2. *J. Geophys. Res.* **82**, 4559–4574.

Kieffer, H. H., S. C. Chase, E. D. Miner, F. D. Palluconi, G. Munch, G. Neugebauer, and T. Z. Martin 1976a. Infrared thermal mapping of the martian surface and atmosphere: First results. *Science* **193**, 780–786.

Kieffer, H. H., P. R. Christensen, T. Z. Martin, E. D. Miner, and F. D. Palluconi 1976b. Temperatures of the martian surface and atmosphere: Viking observation of diurnal and geometric variations. *Science* **194**, 1346–1351.

Jakosky, B. M., and T. Z. Martin 1987. Mars: North-polar atmospheric temperatures during dust storms. *Icarus* **72**, 528–534.

James, P. B., J. F. Bell III, R. T. Clancy, S. W. Lee, L. J. Martin, and M. J. Wolff 1996. Global imaging of Mars by Hubble Space Telescope during the 1995 opposition. *J. Geophys. Res.* **101**, 18883–18890.

Leovy, C. B. 1982. Martian meteorological variability. *Adv. Space Res.* **2**, 19–44.

Leovy, C. B. 1985. The general circulation of Mars: Models and observations. *Adv. Geophys.* **28a**, 327–346.

Leovy, C. B., and R. W. Zurek 1979. Thermal tides and martian dust storms: Direct evidence for coupling. *J. Geophys. Res.* **84**, 2956–2968.

Lindal, G. F., H. B. Hotz, D. N. Sweetnam, Z. Shippony, J. P. Brenkle, G. V. Hartsell, R. T. Spear, and W. H. Michael 1979. Viking radio occultation measurements of the atmosphere and topography on Mars. *J. Geophys. Res.* **84**, 8443–8456.

Martin, L., and R. W. Zurek 1993. An analysis of the history of dust activity on Mars. *J. Geophys. Res.* **98**, 3221–3246.

Martin, T. Z. 1981. Mean thermal and albedo behavior of the Mars surface and atmosphere over a martian year. *Icarus* **45**, 427–446.

Martin, T. Z. 1986. Thermal infrared opacity of the Mars atmosphere. *Icarus* **66**, 2–21.

Martin, T. Z., and H. Kieffer 1979. Thermal infrared properties of the martian atmosphere, 2: The 15 μm band measurements. *J. Geophys. Res.* **84**, 2843–2852.

Martin, T. Z., and M. I. Richardson 1993. New dust opacity mapping from Viking infrared thermal mapper data. *J. Geophys. Res.* **98**, 10941–10949.

Martin, T. Z., A. R. Peterfreund, E. D. Miner, H. H. Kieffer, and G. E. Hunt 1979. Thermal infrared properties of the martian atmosphere, 1: Global behavior at 7, 9, 11, and 20 μm. *J. Geophys. Res.* **84**, 2830–2842.

Michelangeli, D. V., O. B. Toon, R. H. Haberle, and J. B. Pollack 1993. Numerical simulations of the formation and evolution of water ice clouds in the martian atmosphere. *Icarus* **102**, 261–285.

Palluconi, F. D., and H. H. Kieffer 1981. Thermal inertia mapping of Mars from 60S to 60N. *Icarus* **45**, 415–426.

Pearl, J. C., B. J. Conrath, M. D. Smith, J. L. Bandfield, and P. R. Christensen 1999. Mars Global Surveyor Thermal Emission Spectrometer observations of ice clouds during aerobraking and science phasing. *J. Geophys. Res.*, submitted.

Pirraglia, J. A., and B. J. Conrath 1974. Martian tidal pressure and wind fields obtained from the Mariner 9 infrared spectroscopy experiment. *J. Atmos. Sci.* **31**, 318–329.

Pollack, J. B., D. S. Colburn, F. M. Flasar, R. Kahn, C. E. Carlston, and D. E. Pidek 1979. Properties and effects of dust particles suspended in the martian atmosphere. *J. Geophys. Res.* **84**, 2929–2946.

Pollack, J. B., M. E. Ockert-Bell, and M. K. Shepard 1995. Viking Lander image analysis of martian atmospheric dust. *J. Geophys. Res.* **100**, 5235–5250.

Richardson, M. I. 1998. Comparison of microwave and infrared measurements of martian atmospheric temperatures: Implications for short-term climate variability. *J. Geophys. Res.* **103**, 5911–5918.

Rodin, A. V., R. T. Clancy, R. J. Wilson, and M. J. Wolff 1999. Thermal feedback between dust and water ice clouds in the Mars atmosphere: Implications for the aphelion climate. *Icarus*, submitted.

Santee, M. L., and D. Crisp 1993. The thermal structure and dust loading of the martian atmosphere during late southern summer: Mariner 9 revisited. *J. Geophys. Res.* **98**, 3261–3279.

Schneider, E. K. 1983. Martian great dust storms: Interpretive axially symmetric models. *Icarus* **55**, 302–331.

Schofield, J. T., J. R. Barnes, D. Crisp, R. M. Haberle, S. Larsen, J. A. Magalhaes, J. R. Murphy, A. Seiff, and G. Wilson 1997. The Mars Pathfinder atmospheric structure investigation/meteorology (ASI/MET) experiment. *Science* **278**, 1752–1758.

Savijarvi, H. 1995. Mars boundary layer modeling: Diurnal moisture cycle and soil properties at the Viking Lander 1 site. *Icarus* **117**, 120–127.

Savijarvi, H. 1999. A model study of the atmospheric boundary layer in the Mars Pathfinder lander conditions. *Q. J. R. Meteorol. Soc.* **125**, 483–493.

Sieff, A., and D. B. Kirk 1977. Structure of the atmosphere of Mars in summer at mid-latitudes. *J. Geophys. Res.* **82**, 4364–4378.

Tamppari, L. K., R. W. Zurek, and D. A. Paige 2000. Viking era water ice clouds. *J. Geophys. Res.* **105**, 4087–4107.

Tillman, J. E. 1988. Mars global atmospheric oscillations: Annually synchronized, transient normal-mode oscillations and the triggering of global dust storm. *J. Geophys. Res.* **93**, 9433–9451.

Toigo, A. D., and M. I. Richardson 2000. Seasonal variation of aerosols in the martian atmosphere. *J. Geophys. Res.* **105**, 4109–4122.

Wilson, R. J. 1997. A general circulation model simulation of the martian polar warming. *Geophys. Res. Lett.* **24**, 123–127.

Wilson, R. J., and K. P. Hamilton 1996. Comprehensive model simulation of thermal tides in the martian atmosphere. *J. Atmos. Sci.* **53**, 1290–1326.

Zurek, R. W. 1976. Diurnal tide in the martian atmosphere. *J. Atmos. Sci.* **33**, 321–337.

Zurek, R. W. 1981. Inference of dust opacities for the 1977 martian great dust storms from Viking Lander 1 pressure data. *Icarus* **45**, 202–215.

Zurek, R. W. 1982. Martian great dust storms: An update. *Icarus* **50**, 288–310.

Zurek, R. W. and C. B. Leovy 1981. Thermal tides in the dusty martian atmosphere: A verification of theory. *Science* **213**, 437–439.

Zurek, R. W., J. R. Barnes, R. M. Haberle, J. B. Pollack, J. E. Tillman, and C. B. Leovy 1992. Dynamics of the atmosphere of Mars. In *Mars* (H. H. Kieffer, B. M. Jakosky, C. W. Snyder, and M. S. Matthews, Eds.), pp. 835–933. Univ. of Arizona Press, Tucson.